BOUND-STATE ENERGIES AND PHASE TRANSITIONS IN GRAPHENE-LIKE STRUCTURES

by

Kelly Cheung

B.A.Sc., University of British Columbia, 2004

M.Sc., University of British Columbia, 2006

A Thesis submitted in partial fulfillment
of the requirements for the degree of

Doctor of Philosophy

in the
Department of Physics
Faculty of Science

Simon Fraser University
Summer 2012

APPROVAL

Name: Kelly Cheung

Degree: Doctor of Philosophy

Title of Thesis: Bound-State Energies and Phase Transitions in Graphene-Like Structures

Examining Committee: Dr. J. Steven Dodge, Chair
Associate Professor

Dr. Igor Herbut, Senior Supervisor
Professor

Dr. Malcolm Kennett, Supervisor
Associate Professor

Dr. Levon Pogosian, Supervisor
Associate Professor

Dr. Howard Trottier, Internal Examiner
Professor

Dr. Mona Berciu, External Examiner
Associate Professor
University of British Columbia

Date Approved: June 22, 2012

Partial Copyright Licence

Abstract

Graphene has been actively researched because its low energy electronic Hamiltonian is the relativistic Dirac equation with vanishing rest mass. Graphene was first fabricated in 2004 by Geim and Novoselov. Although graphene is a semi-metal, electronic applications require knowledge of how to change its phase from a semi-metal to an insulator. For spinless fermions on graphene, fermion density imbalance, coupling between its Dirac points, and directed next nearest neighbor hopping can lead to charge density wave, Kekule bond density wave, and quantum Hall insulating phases. Furthermore, topological defects such as line defects and vortices allow bound state solutions within the gap giving rise to fractional charge. The results are not only applicable to graphene, but can also be applied in general to fermions on a hexagonal lattice.

Another example where a Dirac linear dispersion is found is for spinless fermions at one-third filling on the Lieb lattice. Fermion density imbalance, staggered nearest neighbour hopping, and directed next nearest neighbor hopping can change this lattice from a semi-metal to an insulating phase characterized by a charge density wave, staggered hopping, broken pi/2 rotation symmetry, or broken time reversal symmetry. By adding and adjusting the strengths of nearest and next nearest neighbour interactions, many of these interesting phases can be energetically favourable in mean-field theory.

Keywords: Graphene; Lieb lattice; topological defects; interactions; phases; Dirac

I dedicate this thesis to my wife Cindy for her patience, understanding, and support.

"When nothing seems to help, I go look at a stonecutter hammering away at his rock perhaps a hundred times without as much as a crack showing in it. Yet at the hundred and first blow it will split in two, and I know it was not that blow that did it, but all that had gone before."

— *Jacob Riis*

Acknowledgments

Firstly, I would like to thank Dr. Igor Herbut for sharing his ideas. He introduced me to all the concepts in this thesis, most notably, graphene, the Lieb lattice, and topological defects. I am sincerely grateful for the opportunity to work with him and for his time during the past 6 years.

I would like to thank Dr. Malcolm Kennett, Dr. Levon Pogosian, and Dr. Chi-Ken Lu for learning about my work and providing critical feedback. Thanks to Dr. J. Steven Dodge and Rose Evans for their assistance allowing me to focus on completing this degree. Many thanks to fellow office mates for their friendship and humour: Dr. Bitan Roy, Peter Smith, Yiwei Zhang, Nazanin Komeilizadeh, Ricky Chu, Hildur Knuttsdottir, Sebastian Cogswell, and Firuz Demir.

It was an honour to teach with Dr. Michael Chen, Dr. Andrew DeBenedictis, Dr. Simon Watkins, Dr. Sarah Johnson, Dr. Cameron Forde, and Dr. Bernd Stelzer. Thanks to David Lee and Mehrdad Rastan for providing computer and lab support allowing me to work with students without worrying about equipment problems. Also thanks to Dr. Barbara Frisken for giving me the opportunity to be a head teaching assistant and to Jen Chang for all her work especially for the teaching assistants.

Lastly, thank you to my wife, my parents, my brother, and my in-laws for their moral support throughout this entire ordeal.

Contents

Approval ii

Abstract iii

Dedication iv

Quotation v

Acknowledgments vi

Contents vii

List of Tables ix

List of Figures x

Preface xii

1 Graphene 1

1.1 Interesting Properties of Graphene 1

1.2 Fabricating Graphene 2

1.3 Graphene Applications 3

1.4 Graphene Hamiltonian 4

1.5 Summary 13

2 Topological Defects in Graphene 14

2.1 Fractional Charge due to Topological Defects 14

2.2 Staggered Chemical Potential 15

2.3 Domain Wall . . . 17
2.4 Kekulé Pattern . . . 21
2.5 Kekulé Pattern: r-independent Vortices . . . 22
2.6 Kekulé Pattern: r-dependent Vortices . . . 26
2.7 Non-zero CDW and KBDW Order Parameters . . . 36
2.8 Quantum Hall State . . . 38
2.9 Non-zero CDW, KBDW, QHE Order Parameters . . . 41
2.10 NN and NNN Interactions . . . 41
2.11 Spinful Hamiltonian . . . 43
2.12 Superconductivity . . . 44
2.13 Summary . . . 44

3 Phases on the Lieb Lattice **46**
3.1 Lieb Lattice . . . 46
3.2 Nearest Neighbour (NN) Interaction . . . 48
3.3 Next Nearest Neighbour (NNN) Interaction . . . 54
3.4 NN and NNN Interactions . . . 55
3.5 Summary . . . 57

Bibliography **60**

List of Tables

2.1 Bound State Energies for $\Delta_0 = 1$ 24
2.2 Degeneracies for $\Delta_0 = 1$ and $p = 1$ 25
2.3 Degeneracies for $\Delta_0 = 1$ and $p = 2$ 25
2.4 Bound State Energies for $\Delta_0 = r$ and $p = 1$ 31
2.5 First Pattern for $\Delta_0 = r$ and $p = 1$ 31
2.6 Second Pattern for $\Delta_0 = r$ and $p = 1$ 31
2.7 First Pattern for $\Delta_0 = r$ and $p = 2$ 32
2.8 Second Pattern for $\Delta_0 = r$ and $p = 2$ 32
2.9 Bound State Energies for $\Delta_c = 1$ and $p = 1$ 36
2.10 Bound State Energies for $\Delta_c = 3$ and $p = 1$ 36
2.11 Bound State Energies for a Meron 39

List of Figures

1.1 Graphene 5
1.2 Wigner-Seitz cell of Graphene 5
1.3 Parallelogram Brillouin zone for Graphene 8
1.4 Energy Dispersion of Graphene 9

2.1 Graphene with Staggered Chemical Potential 16
2.2 Graphene with Line Defect 18
2.3 Spinor in y due to a Line Defect in y with $|p_x| < \sqrt{E^2 - m_1^2}$ 20
2.4 Bound Spinor in y due to a Line Defect in y for $\pm p_x = E$ 20
2.5 Kekulé Pattern with $\delta t_{r,r+s_i} = \Delta e^{i\vec{k}^+ \cdot \vec{s}_i} e^{i\vec{G}\cdot\vec{r}}/3 + c.c.$ 21
2.6 Radial Components for for $\Delta_0 = 1$ and $p = 1$ 27
2.7 Radial Components for for $\Delta_0 = 1$ and $p = 2$ 28
2.8 Radial Components for for $\Delta_0 = 1$, $p = 1$, and $n = 0$ 29
2.9 Radial Components for $\Delta_0 = r$ and $p = 1$ 33
2.10 Radial Components for $\Delta_0 = r$ and $p = 2$ 34
2.11 Meron 38
2.12 Skyrmion 39
2.13 Graphene with Directed NNN hopping 40

3.1 Lieb Lattice 47
3.2 Energy Dispersion of Lieb Lattice 48
3.3 Energy Dispersion with NN interaction in Hartree Channel 50
3.4 Order Parameter for NN interaction in Hartree Channel 50
3.5 CDW in Lieb Lattice 51
3.6 Staggered Hopping in Lieb Lattice 52

3.7 Energy Dispersion with Staggered NN Hopping in the Fock Channel 53
3.8 Order Parameter with Staggered NN Hopping in the Fock Channel 53
3.9 Directed NNN hopping in Lieb Lattice 55
3.10 Energy Dispersion with NNN interaction in the Hartree Channel 56
3.11 Order Parameters with NNN interaction in the Hartree Channel 56
3.12 Phase Diagram for the Lieb Lattice 57
3.13 Order Parameters for NN and NNN interactions with $V_2/t = 0.4$ 58

Preface

The work in this thesis was first inspired by Hou, Chamon, and Mudry [25]. Their paper revealed that a Kekulé hopping pattern in graphene with a vortex in its order parameter not only created an insulating state, but also produced zero energy states that could lead to fractional charge. Seradjeh [50] then analytically examined a vortex with vorticity one and found some of the bound state solutions where the order parameter goes as r or is constant. This thesis explores all of the bound state solutions that occur for any vorticity and provides a method to solve any radial profile in the vortex order parameter. Furthermore, other topological defects that can lead to bound state solutions in graphene are explored. The Lieb lattice, which has a similar energy dispersion to graphene but with an additional flat band, is also examined. To consider the possibility of interesting phases on graphene and the Lieb lattice, nearest neighbour and next nearest neighbour interactions are added to the Hamiltonian and solved in mean-field theory. Phase diagrams are found from minimizing the free energy with respect to the order parameters.

In the first chapter, a brief history of graphene, its properties, and possible applications are explored. The second chapter discusses the mass matrices that change graphene from a semi-metal to an insulator. Moreover, bound state solutions are found for particular choices of the order parameters. In the third chapter, the possible phases of spinless fermions at one-third filling on the Lieb lattice are discussed. The strengths of nearest neighbour and next nearest neighbour interactions lead to energetically favourable insulating phases.

Chapter 1

Graphene

1.1 Interesting Properties of Graphene

Graphene, a flat two dimensional layer of carbon atoms in a hexagonal lattice, is fascinating because its low energy quasiparticles are described by the Dirac equation rather than the Schrodinger equation. Specifically, the quasiparticles are governed by a (2+1) dimensional Dirac equation with an effective speed of light of $v_F \approx 10^6$ m/s (300 times less than the speed of light). The energy dispersion in graphene was first discovered to be linear in momentum by Wallace [54] in 1947 when he examined the band structure of graphite. He ignored the interactions between planes in the tight-binding model since the spacing between the layers of graphite (3.37 Å) is much larger than the spacing between carbon atoms in the same layer (1.42 Å). In 2004, Geim and Novoselov [41] were the first to fabricate, identify, and characterize graphene. For their efforts, they received the Nobel Prize in Physics in 2010.

The mechanical and electrical properties of graphene are unique, and they can be exploited for many applications, most notably in electronics. Mobility (defined as the ratio of conductivity to the electronic charge multiplied by charge carrier density) in graphene is comparable to undoped Indium Antimonide (InSb), which has the largest room temperature mobility of any presently known semiconductor: $77,000$ cm^{2}V^{-1}s^{-1} at room temperature [44]. In graphene, mobility is experimentally found to be between $55,000 - 125,000$ cm^{2}V^{-1}s^{-1} for charge carrier densities of 4.3×10^{10} cm^{-2} at room temperature and $80,000 - 260,000$ cm^{2}V^{-1}s^{-1} at 5 K for densities of 0.8×10^{10} cm^{-2} [64]. Moreover, its mobility stays high ($18,000 - 46,000$ cm^{2}V^{-1}s^{-1}) even for high carrier concentrations (10^{12} cm^{-2}) at room temperature.

In addition, graphene exhibits an anomalous quantum Hall effect. Two dimensional electron systems exhibit the Hall effect (first discovered in 1879) where the combination of an in-plane current and transverse magnetic field, B, causes a potential drop perpendicular to the current and magnetic field [20]. The ratio of the current flowing to the potential drop (Hall conductivity) is directly proportional to the magnetic field. In particular, the energy levels for electrons in a magnetic field are quantized in (Landau) levels $E_N = (N + 1/2)\hbar eB/mc$ where N is a non-negative integer. The Hall conductivity was found by von Klitzing [53] to be quantized: $\sigma_{xy} = Ne^2/h$ where e is the electric charge and h is the Planck constant. This is also known as the interger quantum Hall effect (QHE). For these results, he was awarded the Nobel Prize in Physics in 1985. The energy levels of quasiparticles in graphene are at $\pm v_F\sqrt{2e\hbar BN/c}$, and the Hall conductivity is $\pm(N + 1/2)4e^2/h$ [62]. Comparing the conductivities, the multiple of 4 difference is due to both the spin degeneracy and the inversion symmetry of the graphene lattice, while the shift by 1/2 in graphene is caused by a Berry's phase of π (wavefunction changes sign when rotated by 360 degrees).

1.2 Fabricating Graphene

In 2004, Geim and Novoselov were able to create graphene by mechanical exfoliation: using adhesive tape to repeatedly split graphite crystals into increasingly thinner pieces. Acetone was then used to dissolve the tape leaving only graphite flakes. After, the flakes were put on a silicon wafer coated with a 300 nm thick silicon oxide film, and an optical microscope was used to search for graphene. A single layer of graphene has a different optical contrast when compared to graphitic crystals with two or more layers. Since then, various techniques have been used in an attempt to more efficiently create larger sheets of graphene.

One method involves graphene growth on silicon carbide. The surface of silicon carbide is first prepared by oxidation or hydrogen gas etching. After, the oxide is removed by heating the sample by electron bombardment to $\approx$ 1000 °C. Then, silicon is removed by increasing the temperature to 1250-1450 °C. This leaves thin graphite layers with the thickness determined by the temperature [5]. Recently, Emtsev *et al.* [13] have shown that graphene mobility can be increased by annealing the samples in argon gas at higher temperatures leading to surface restructuring before graphene is formed.

Another technique is to grow graphene epitaxially on transition metal substrates. The metal substrate is heated to temperatures higher than 1000 °C while being exposed to a

carbon-rich gas. The carbon atoms then diffuse into the metal crystal. When the metal is cooled, the carbon atoms move to the surface of the metal forming layers of graphene depending on the amount of carbon atoms absorbed. Examples are graphene on iridium in ethylene gas [11], on nickel in methane gas [42], and on copper in methane gas [36].

Most recently, diffusion-assisted synthesis has been used to create graphene at lower temperatures [32]. In this method, nickel film is deposited onto a substrate such as glass. A paste of graphite powder is then pressed against the nickel surface forcing the carbon into the nickel. After being heated at temperatures between 25-260 °C in air or argon gas, graphene is left on the substrate after etching away the nickel-carbon surface.

1.3 Graphene Applications

Due to graphene's unique properties, graphene is envisioned to improve many devices. Graphene can lead to fast transistors due to its high mobility. Even though graphene is atomically thin, the behaviour of resistivity, Hall coefficient, surface charge density, and Fermi energy in graphene transistors are similar to the ambipolar field effect in semiconductors without a zero conductance region [41]. Recently, IBM has created a graphene transistor with a cut-off frequency of 155 GHz [58]. They formed graphene through epitaxial growth on copper foil exposed to ethylene gas at 975 °C. It was then transferred onto a diamond-like carbon film that was grown on silicon oxide using cyclohexane (C_6H_{12}).

Another application for graphene is touch screens. Currently, indium tin oxide is being used for touch screens because it is transparent and conductive. Unfortunately, indium is hard-to-find, expensive, and brittle. Graphene with its high electrical conductivity, high optical transparency (absorbs 2.3 percent of white light) [39], high breaking strength (42 N/m) [34], and flexibility (maintains performance after being stretched by 5 %) [35] is being examined as a replacement for indium tin oxide. In these applications, graphene is placed on top of a metal grid such as aluminum on a flexible substrate such as glass [63]. Also, graphene is being researched to replace indium tin oxide in organic light emitting diodes (OLED) [57] and in solar cells [55].

Graphene is also used in chemical vapour sensors. The adsorption of individual gas molecules on the surface of graphene leads to a detectable change in its electrical resistance. A recent set-up involves creation of a free-standing graphene foam which allows gases to easily adsorb onto its huge surface area [10]. Nickel foam is heated in methane gas to

create graphene. A layer of PMMA (polymethyl methacrylate) is deposited on the surface of graphene as the nickel is dissolved with hydrochloric acid or ferric chloride. The PMMA is then removed with acetone. This sensor is able to measure ammonia and nitrogen dioxide at concentrations as small as 20 parts per million which is ten times more sensitive than commercially available conducting polymer sensors [60].

1.4 Graphene Hamiltonian

Carbon has six electrons; the two $1s$ electrons are inert and do not participate in bonding. In graphene, three of the electrons $(2s, 2p_x, 2p_y)$ hybridize and form three planar sp^2 orbitals. Each of these orbitals have one electron. The overlap of these new orbitals with nearby carbon atoms create three strong covalent (σ) bonds resulting in the hexagonal lattice. The other $2p_z$ electron forms weaker covalent (π) bonds with neighbouring atoms, and these electrons, one per lattice site, are responsible for the electronic properties of graphene.

Graphene can be viewed as a triangular Bravais lattice with a 2-point basis as shown in Fig. 1.1. The primitive lattice vectors are $\vec{a}_1 = (\sqrt{3}, 3)(a/2)$ and $\vec{a}_2 = (\sqrt{3}, -3)(a/2)$ where $\sqrt{3}a$ is the lattice spacing. There are three vectors that connect sites 1 to site 2: $\vec{s}_1 = (0, -a)$, $\vec{s}_2 = (\sqrt{3}, 1)(a/2)$, and $\vec{s}_3 = (-\sqrt{3}, 1)(a/2)$. The reciprocal primitive lattice vectors are $\vec{b}_1 = (\sqrt{3}/2, 1/2)(4\pi/3a)$ and $\vec{b}_2 = (\sqrt{3}/2, -1/2)(4\pi/3a)$ with the Wigner-Seitz cell shown in Fig. 1.2.

The Schrödinger equation for an electron in an atomic potential U localized at $\vec{r}_a$ is

$$H^{(a)} = -\frac{\hbar^2}{2m}\vec{\nabla}^2 + U_{r_a} \tag{1.1}$$

with atomic wavefunctions $\langle r|\, n, r_a\rangle$ with quantum numbers n. For an electron in a periodic array of atomic potentials,

$$H^{(pp)} = H^{(a)} + \sum_{a\neq b} U_{r_b}\,. \tag{1.2}$$

Therefore,

$$\begin{aligned}
\langle n, r_a|\, H^{(pp)}|\, m, r_a\rangle &= \langle n, r_a|\, H^{(a)}|m, r_a\rangle + \sum_{a\neq b}\langle n, r_a|\, U_{r_b}|\, m, r_a\rangle \\
&= E_n\delta_{n,m} + \sum_{a\neq b}\langle n, r_a|\, U_{r_b}|\, m, r_a\rangle \\
&= E_n\delta_{n,m} + 0\,,
\end{aligned} \tag{1.3}$$

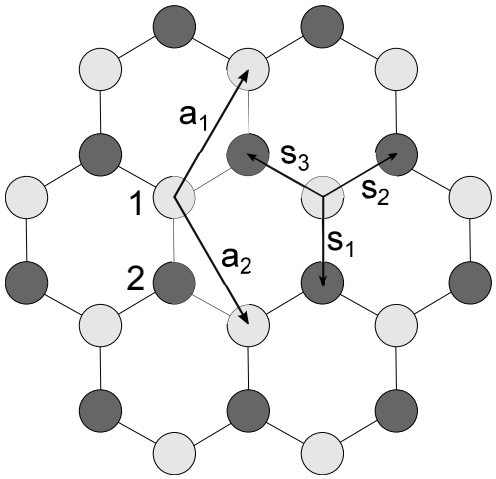

Figure 1.1: Graphene is a monolayer of carbon atoms in a hexagonal lattice: a triangular Bravais lattice with a 2 point basis: 1 (light), 2 (dark). The primitive lattice vectors are $\vec{a}_1 = (\sqrt{3}, 3)(a/2)$ and $\vec{a}_2 = (\sqrt{3}, -3)(a/2)$ where $\sqrt{3}a$ is the lattice spacing. Sites 1 and 2 are connected by three vectors: $\vec{s}_1 = (0, -a)$, $\vec{s}_2 = (\sqrt{3}, 1)(a/2)$, and $\vec{s}_3 = (-\sqrt{3}, 1)(a/2)$.

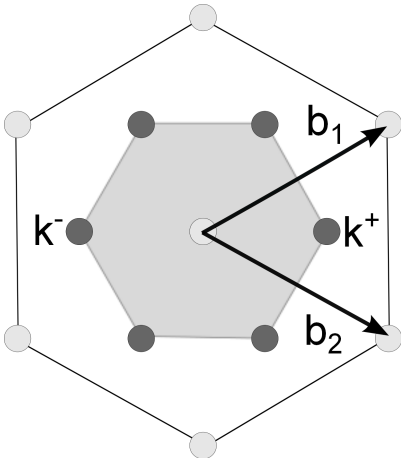

Figure 1.2: The reciprocal lattice of graphene has reciprocal primitive lattice vectors $\vec{b}_1$ and $\vec{b}_2$; the light dots are reciprocal lattice points. The Wigner-Seitz cell (first Brillouin zone), showing the points closer to a single lattice point than any other point, is the shaded hexagon. There are 6 Dirac points (dark) but only two are inequivalent (not related by a reciprocal lattice vector). They are labelled k^+ and k^-.

where E_n is the energy of the atomic state, and δ is the Dirac delta function. The second term on the right hand side is taken to be zero because the overlap of atomic wavefunctions with a potential from a different atom is small.

For wavefunctions localized at different atoms $a \neq b$,

$$\begin{aligned} \langle n, r_a | \, H^{(pp)} | \, m, r_b \rangle &= \langle n, r_a | \, H^{(a)} | \, m, r_b \rangle + \sum_{a \neq c} \langle n, r_a | \, U_{r_c} | \, m, r_b \rangle \\ &= 0 - t_{r_a, r_b} \delta_{n,m} \, , \end{aligned} \tag{1.4}$$

where the hopping parameter $-t_{r_a,r_b}$ is taken to be non-zero only if atoms on sites $\vec{r}_a$ and $\vec{r}_b$ are nearest neighbours since atomic wavefunctions are localized near their potentials. In addition, hopping between different orbitals is taken to be negligibly small due to different symmetries. The first term on the right can only be non-zero for $a = b$.

Hence, the Hamiltonian can be rewritten in second quantized form as:

$$H^{(pp)} = \sum_i E_i c^\dagger_{r_i} c_{r_i} - \sum_{i \neq j} t_{r_i, r_j} c^\dagger_{r_i} c_{r_j} \tag{1.5}$$

where $c^\dagger_{r_j}$ (c_{r_j}) are the fermionic creation (annihilation) operators at $\vec{r}_j$ satisfying $\{c_{r_i}, c^\dagger_{r_j}\} = \delta_{i,j}$. Shifting the energy by $-\sum_i E_i$, the tight-binding Hamiltonian for spinless fermions on the hexagonal lattice is:

$$H_0 = - \sum_{r \in \Lambda_1} \sum_{i=1}^{3} t_{r, r+s_i} c^\dagger_{1,r} c_{2, r+s_i} + h.c. \tag{1.6}$$

where Λ_1 contains all points $\sum_{j=1}^{2} n_j \, \vec{a}_j$ where $\{n_j \in \mathbb{N}_1 : n_j \leq N_j\}$ with N_j specifying the size of the lattice, and $c^\dagger_{z,r_j}$ (c_{z,r_j}) are the fermionic creation (annihilation) operators for site z at $\vec{r}_j$.

In graphene, $t = t_{r,r+s_i} \approx 3$ eV [47]. The Hamiltonian is invariant under T_{a_j}, the set of translations by a primitive lattice vector $\vec{a}_i$, since the hopping parameter is independent of

position:

$$\begin{aligned} T_{a_j} H_0 T_{a_j}^\dagger &= T_{a_j}(-\sum_{r\in\Lambda_1}\sum_{i=1}^{3} t\, c_{1,r}^\dagger c_{2,r+s_i} + h.c.)\, T_{a_j}^\dagger \\ &= -\sum_{r\in\Lambda_1}\sum_{i=1}^{3} t\, c_{1,r+a_j}^\dagger c_{2,r+s_i+a_j} + h.c. \\ &= -\sum_{r'\in\Lambda_1}\sum_{i=1}^{3} t\, c_{1,r'}^\dagger c_{2,r'+s_i} + h.c. \\ &= H_0\,, \end{aligned} \tag{1.7}$$

where $\vec{r}' = \vec{r} - \vec{a}_j$. Similarly, the Hamiltonian is invariant under time reversal T since the hopping parameter is a real number.

$$\begin{aligned} T H_0 T^\dagger &= T(-\sum_{r\in\Lambda_1}\sum_{i=1}^{3} t\, c_{1,r}^\dagger c_{2,r+s_i} + h.c.)\, T^\dagger \\ &= -\sum_{r\in\Lambda_1}\sum_{i=1}^{3} t\, c_{1,r}^\dagger c_{2,r+s_i} + h.c. \\ &= H_0\,, \end{aligned} \tag{1.8}$$

since $T c_{j,r_j} T^\dagger = c_{j,r_j}$.

The Fourier transform of the operators is defined using the Brillouin zone shown in Fig. 1.3:

$$c_{j,r}^\dagger = \frac{1}{\sqrt{|\Lambda_1|}} \sum_{\vec{k}'} e^{-i\vec{k}'\cdot\vec{r}} c_{j,k'}^\dagger\,, \tag{1.9}$$

where $\vec{k}' = \sum_{i=1}^{2} \frac{n_i'}{N_i}\vec{b}_i$ with $\{n_i' \in \mathbb{N}_1 : n_i' \le N_i\}$, and the number of site 1 is $|\Lambda_1| = \Pi_{i=1}^{2} N_i$. The Hamiltonian becomes $H_0 = \sum_k \Psi_k^\dagger H_k^{(0)} \Psi_k$ where

$$\begin{aligned} H_k^{(0)} &= -t \begin{pmatrix} 0 & \Phi_k \\ \Phi_k^* & 0 \end{pmatrix} \\ &= -t\,(\sigma_1 \sum_{i=1}^{3} \cos(\vec{k}\cdot\vec{s}_i) - \sigma_2 \sum_{i=1}^{3} \sin(\vec{k}\cdot\vec{s}_i))\,, \end{aligned} \tag{1.10}$$

where $\Phi_k = \sum_{i=1}^{3} e^{i\vec{k}\cdot\vec{s}_i}$, $\Psi_k^\dagger = (c_{1,k}^\dagger, c_{2,k}^\dagger)$, σ_0 is the 2×2 identity matrix, and $\vec{\sigma}$ are the Pauli matrices defined by $\{\sigma_\mu, \sigma_\nu\} = 2\delta_{\mu,\nu}\,\sigma_0$ with $\{\cdot,\cdot\}$ being the anticommutator:

$$\sigma_1 = \begin{pmatrix} 0 & 1 \\ 1 & 0 \end{pmatrix},\ \sigma_2 = \begin{pmatrix} 0 & -i \\ i & 0 \end{pmatrix},\ \sigma_3 = \begin{pmatrix} 1 & 0 \\ 0 & -1 \end{pmatrix}. \tag{1.11}$$

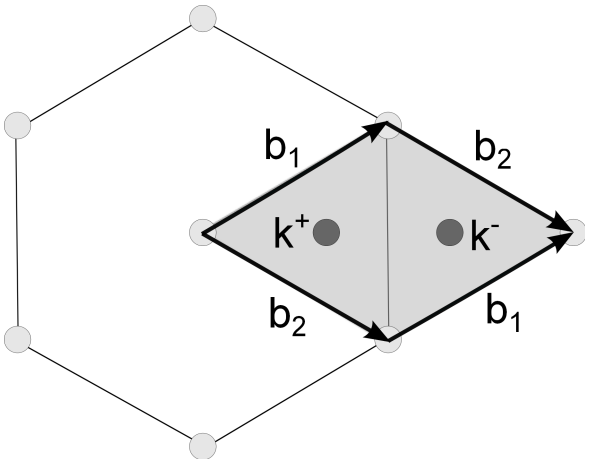

Figure 1.3: Another choice of the Brillouin zone is a parallelogram (shaded) with its sides determined by $\vec{b}_1$ and $\vec{b}_2$. The light dots are reciprocal lattice points, and the dark dots are the two Dirac points.

The energy spectrum must be symmetric about zero energy because σ_3 anticommutes with the Hamiltonian. For Ψ_k that solves the Hamiltonian with energy eigenvalue E, $\sigma_3\Psi_k$ solves the Hamiltonian with energy -E:

$$\begin{aligned} H_k^{(0)}\left(\sigma_3\Psi_k\right) &= -\sigma_3 H_k^{(0)}\Psi_k \\ &= -\sigma_3 E\Psi_k \\ &= -E\left(\sigma_3\Psi_k\right). \end{aligned} \tag{1.12}$$

Solving for the energy eigenvalues, the energy bands for $H_k^{(0)}$ are:

$$E = \pm t|\Phi_k| = \pm t\sqrt{3 + 2\cos(\sqrt{3}k_x a) + 4\cos(\sqrt{3}k_x a/2)\cos(3k_y a/2)}\,, \tag{1.13}$$

and are shown in Fig. 1.4. Considering spin, each site can be filled with two electrons. Since graphene has one electron for each site, half of the states are filled. Therefore at zero temperature, only the bottom band is filled. The two bands touch at two Dirac points: $k^+ = (1/\sqrt{3}, 0)(4\pi/3a)$ and $k^- = (2/\sqrt{3}, 0)(4\pi/3a)$ where the energy is zero, and therefore, the Fermi surface consists only of these two points.

For low energy excitations in graphene, the behaviour is governed by momenta near k^+

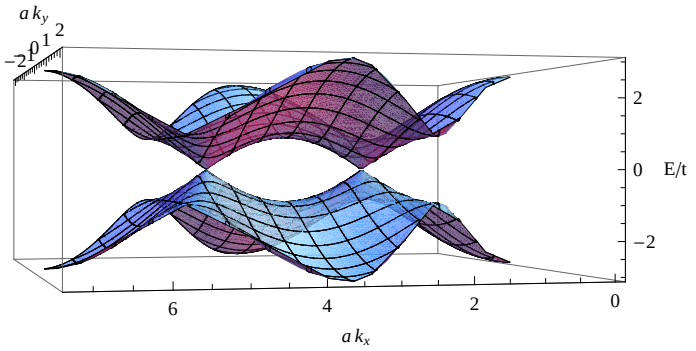

Figure 1.4: The energy dispersion of graphene consists of two bands which touch at two Dirac points: $k^+ = (1/\sqrt{3}, 0)(4\pi/3a)$ and $k^- = (2/\sqrt{3}, 0)(4\pi/3a)$.

and k^-. Therefore, in the continuum limit ($a \to \infty$), the Hamiltonian can be written as:

$$H_0 \approx \sum_{|\vec{p}|<P} \Psi^\dagger_{k^-+p} H^{(0)}_{k^-+p} \Psi_{k^-+p} + \Psi^\dagger_{k^++p} H^{(0)}_{k^++p} \Psi_{k^++p}\,, \tag{1.14}$$

where P is a cutoff. Expanding in the first two orders of $\vec{p}$ near $k^\pm$,

$$\Phi_{k^\pm+p} = (3a/2)(\mp p_x - i p_y) + (3a^2/8)(p_x^2 - p_y^2) + (3a^2/4)(\mp i p_x p_y))\,. \tag{1.15}$$

The second order terms are the same order or larger than the first order when $|\vec{p}| \geq 2/a$ which determines the cutoff P. To first order, the Hamiltonian becomes $H_0 = \sum_p \Psi^\dagger_p H^{(0)}_p \Psi_p$ where

$$\begin{aligned} H^{(0)}_p &= \hbar v_F \begin{pmatrix} 0 & -p_x - i p_y & 0 & 0 \\ -p_x + i p_y & 0 & 0 & 0 \\ 0 & 0 & 0 & p_x - i p_y \\ 0 & 0 & p_x + i p_y & 0 \end{pmatrix} \\ &= -\sigma_3 \otimes \sigma_1\, p_x + \sigma_0 \otimes \sigma_2\, p_y\,, \end{aligned} \tag{1.16}$$

with $\Psi^\dagger_p = (c^\dagger_{2p-}, c^\dagger_{1p-}, c^\dagger_{2p+}, c^\dagger_{1p+})$ where $c_{jp\pm} = c_{j,k^\pm+p}$ is the annihilation operator at $\vec{r}_j$ with momentum $\vec{k}^\pm + \vec{p}$, and $v_F = 3at/2\hbar$. Setting both $v_F = 1$ and $\hbar = 1$ for convenience and rewriting the Hamiltonian in the position basis using $\vec{p} = -i\vec{\nabla}$, $H_0 = \int d^2\vec{x}\, \Psi^\dagger H^{(0)} \Psi$

with

$$
\begin{aligned}
H^{(0)} &= \begin{pmatrix} 0 & i\partial_x - \partial_y & 0 & 0 \\ i\partial_x + \partial_y & 0 & 0 & 0 \\ 0 & 0 & 0 & -i\partial_x - \partial_y \\ 0 & 0 & -i\partial_x + \partial_y & 0 \end{pmatrix} \\
&= i\sigma_3 \otimes \sigma_1 \, \partial_x - i\sigma_0 \otimes \sigma_2 \, \partial_y \\
&= -\gamma_0\gamma_1\partial_x - \gamma_0\gamma_2\partial_y \,, \qquad (1.17)
\end{aligned}
$$

where the four component spinor is defined as $\Psi^\dagger = (c^\dagger_{2-}, c^\dagger_{1-}, c^\dagger_{2+}, c^\dagger_{1+})$, I_j is the $j \times j$ identity matrix, and the gamma matrices are defined by $\{\gamma_\mu, \gamma_\nu\} = 2\delta_{\mu,\nu} I_4$.

$$
\gamma_0 = \sigma_0 \otimes \sigma_3 = \begin{pmatrix} 1 & 0 & 0 & 0 \\ 0 & -1 & 0 & 0 \\ 0 & 0 & 1 & 0 \\ 0 & 0 & 0 & -1 \end{pmatrix}, \; \gamma_1 = \sigma_3 \otimes \sigma_2 = \begin{pmatrix} 0 & -i & 0 & 0 \\ i & 0 & 0 & 0 \\ 0 & 0 & 0 & i \\ 0 & 0 & -i & 0 \end{pmatrix},
$$

$$
\gamma_2 = \sigma_0 \otimes \sigma_1 = \begin{pmatrix} 0 & 1 & 0 & 0 \\ 1 & 0 & 0 & 0 \\ 0 & 0 & 0 & 1 \\ 0 & 0 & 1 & 0 \end{pmatrix}, \; \gamma_3 = \sigma_1 \otimes \sigma_2 = \begin{pmatrix} 0 & 0 & 0 & -i \\ 0 & 0 & i & 0 \\ 0 & -i & 0 & 0 \\ i & 0 & 0 & 0 \end{pmatrix},
$$

$$
\gamma_5 = \gamma_0\gamma_1\gamma_2\gamma_3 = \sigma_2 \otimes \sigma_2 = \begin{pmatrix} 0 & 0 & 0 & -1 \\ 0 & 0 & 1 & 0 \\ 0 & 1 & 0 & 0 \\ -1 & 0 & 0 & 0 \end{pmatrix}. \qquad (1.18)
$$

Of particular interest are the four matrices M_1, M_2, M_3, M_4 that anticommute with $H^{(0)}$. M_1, M_2, M_3 also anticommute with each other, but not M_4.

$$
M_1 = \sigma_0 \otimes \sigma_3 = \gamma_0 = \begin{pmatrix} 1 & 0 & 0 & 0 \\ 0 & -1 & 0 & 0 \\ 0 & 0 & 1 & 0 \\ 0 & 0 & 0 & -1 \end{pmatrix},
$$

$$M_2 = \sigma_1 \otimes \sigma_1 = i\gamma_0\gamma_3 = \begin{pmatrix} 0 & 0 & 0 & 1 \\ 0 & 0 & 1 & 0 \\ 0 & 1 & 0 & 0 \\ 1 & 0 & 0 & 0 \end{pmatrix},$$

$$M_3 = \sigma_2 \otimes \sigma_1 = i\gamma_0\gamma_5 = \begin{pmatrix} 0 & 0 & 0 & -i \\ 0 & 0 & -i & 0 \\ 0 & i & 0 & 0 \\ i & 0 & 0 & 0 \end{pmatrix},$$

$$M_4 = \sigma_3 \otimes \sigma_3 = i\gamma_1\gamma_2 = \begin{pmatrix} 1 & 0 & 0 & 0 \\ 0 & -1 & 0 & 0 \\ 0 & 0 & -1 & 0 \\ 0 & 0 & 0 & 1 \end{pmatrix}. \tag{1.19}$$

By rewriting $H^{(0)}, M_1, M_2, M_3, M_4$ in terms of $X_{\mu\nu} = \sigma_\mu \otimes \sigma_\nu$, the anticommuting relationships can be clearly seen. $H^{(0)}$ is a linear combination of X_{31} and X_{02}, while (M_1, M_2, M_3, M_4) are $(X_{03}, X_{11}, X_{21}, X_{33})$. For $X_{\mu\nu}$ to anticommute with $X_{\mu'\nu'}$, either σ_μ must commute with $\sigma_{\mu'}$ and σ_ν must anticommute with $\sigma_{\nu'}$ or vice versa. For example, $M_1 = X_{03}$ anticommutes with the Hamiltonian since σ_0 commutes with σ_3 and σ_0, while σ_3 anticommutes with σ_1 and σ_2. Going through this process reveals the four possible matrices M_j.

Since there are matrices that anticommute with the Hamiltonian, the energy spectrum is symmetric about zero energy. The Hamiltonian $H^{(0)}$ is the relativistic Dirac Hamiltonian with vanishing rest mass. In momentum space, the linear energy dispersion is most easily found by examining the square of the Hamiltonian $H_p^{(0)}$:

$$\begin{aligned} (H_p^{(0)})^2 &= (-\sigma_3 \otimes \sigma_1\, p_x + \sigma_0 \otimes \sigma_2\, p_y)^2 \\ &= I_4\, |\vec{p}|^2\,, \end{aligned} \tag{1.20}$$

since $\sigma_j^2 = \sigma_0$, and X_{31} and X_{02} anticommute. Therefore, $E_p = \pm|\vec{p}|$, and for low energies,

the density of states of each Dirac point $g(E)$ is linear in energy:

$$\begin{aligned} g(E_p) &= \int \frac{d^2\vec{p}}{4\pi^2}\,\delta(|\vec{p}|-E_p) \\ &= \int \frac{p\,dp}{2\pi}\,\delta(p-E_p) \\ &= \frac{E_p}{2\pi}\,. \end{aligned} \tag{1.21}$$

The time reversal operator, $T=\sigma_x\otimes I_2 K$ where K is complex conjugation, switches the Dirac points:

$$T=\sigma_x\otimes I_2 K = i\gamma_1\gamma_5 K = \begin{pmatrix} 0 & 0 & 1 & 0 \\ 0 & 0 & 0 & 1 \\ 1 & 0 & 0 & 0 \\ 0 & 1 & 0 & 0 \end{pmatrix} K\,. \tag{1.22}$$

Because $T^2=1$ and T commutes with $H^{(0)}$, for Ψ that solves the Hamiltonian with energy eigenvalue E, $T\Psi$ also solves it with the same energy:

$$\begin{aligned} H^{(0)}\,(T\Psi) &= TH^{(0)}\Psi \\ &= TE\Psi \\ &= E\,(T\Psi)\,. \end{aligned} \tag{1.23}$$

Decoupling $H^{(0)}\Psi = E\Psi$ gives second-order differential equations because the Dirac points are not coupled at low energies:

$$(-\partial_x^2-\partial_y^2)\,c_{2\pm} = E^2\,c_{2\pm}\,. \tag{1.24}$$

Hence, for a given E with the allowed values of $\vec{p}$ determined by the boundary conditions, the solutions for the four component spinor Ψ are combinations of the following forms:

$$\Psi_{1-}=\begin{pmatrix} e^{ip_x x}\,e^{ip_y y} \\ \frac{(-p_x+ip_y)}{E}\,e^{ip_x x}\,e^{ip_y y} \\ 0 \\ 0 \end{pmatrix},\ \Psi_{1+}=\begin{pmatrix} 0 \\ 0 \\ e^{-ip_x x}\,e^{-ip_y y} \\ \frac{(-p_x-ip_y)}{E}\,e^{-ip_x x}\,e^{-ip_y y} \end{pmatrix},$$

$$\Psi_{2-}=\begin{pmatrix} e^{ip_x x}\,e^{-ip_y y} \\ \frac{(-p_x-ip_y)}{E}\,e^{ip_x x}\,e^{-ip_y y} \\ 0 \\ 0 \end{pmatrix},\ \Psi_{2+}=\begin{pmatrix} 0 \\ 0 \\ e^{-ip_x x}\,e^{ip_y y} \\ \frac{(-p_x+ip_y)}{E}\,e^{-ip_x x}\,e^{ip_y y} \end{pmatrix},$$

$$\Psi_{3-} = \begin{pmatrix} e^{-ip_x x}\, e^{ip_y y} \\ \frac{(p_x+ip_y)}{E}\, e^{-ip_x x}\, e^{ip_y y} \\ 0 \\ 0 \end{pmatrix},\ \Psi_{3+} = \begin{pmatrix} 0 \\ 0 \\ e^{ip_x x}\, e^{-ip_y y} \\ \frac{(p_x-ip_y)}{E}\, e^{ip_x x}\, e^{-ip_y y} \end{pmatrix},$$

$$\Psi_{4-} = \begin{pmatrix} e^{-ip_x x}\, e^{-ip_y y} \\ \frac{(-p_x-ip_y)}{E}\, e^{-ip_x x}\, e^{-ip_y y} \\ 0 \\ 0 \end{pmatrix},\ \Psi_{4+} = \begin{pmatrix} 0 \\ 0 \\ e^{ip_x x}\, e^{ip_y y} \\ \frac{(-p_x+ip_y)}{E}\, e^{ip_x x}\, e^{ip_y y} \end{pmatrix}. \tag{1.25}$$

The solutions are related by the time reversal operator:

$$\Psi_{j\pm} = T\Psi_{j\mp}\,. \tag{1.26}$$

1.5 Summary

Graphene is interesting due to its electronic Hamiltonian being linear in momentum near the two Dirac points. There are two bands due to having two sites per unit cell, and the bands touch at the two Dirac points. Since there is one electron per spin per lattice site, only the lower band is filled resulting in a semi-metallic state. This can lead to many favourable properties such as high carrier mobility for electronic applications. For low energy excitations in the continuum limit, spinless fermions are represented by a four component spinor due to the two lattice sites and the two Dirac points. There are matrices that anticommute with the Hamiltonian, and as a result, the spectrum must be symmetric. Also, the time reversal operator commutes with the Hamiltonian relating spinor solutions with the same energy. Lastly, in this limit, there is no coupling between the two Dirac points, and the solutions can be found analytically from solving two second-order differential equations.

Chapter 2

Topological Defects in Graphene

2.1 Fractional Charge due to Topological Defects

Laughlin, Störmer, and Tsui [33] won a Nobel Prize in Physics in 1998 for discovering and explaining the fractional quantum Hall effect. This was done in a two dimensional system of electrons using strong magnetic fields breaking time-reversal symmetry. Since then, examples of fractional charge without breaking time-reversal are actively being researched. In particular, topological defects such as domain walls and vortices generated by spontaneous symmetry breaking or by placing graphene on certain substrates are being examined. Hou, Chamon, and Mudry [25] found that vortices on a Kekulé hopping texture in graphene lead to fractional charge while preserving time-reversal symmetry. Firstly, they used the fact that electronic charge is conserved in graphene. Moreover, a vortex with vorticity one on a Kekulé texture not only opens a gap at the Dirac points, but also keeps the spectrum symmetric with a single zero energy state. Due to the spectrum being half filled in graphene, the total charge Q when the zero energy state is not filled is $-1/2$ compared to the situation without the defect.

$$\begin{aligned} Q &= \int_{-\infty}^{\infty} d^2\vec{r}\,\rho_r \\ &= -\frac{1}{2}, \end{aligned} \tag{2.1}$$

where ρ_r is the charge density relative to the topologically trivial background:

$$\begin{aligned}\rho_r &= \int_{-\infty}^{0} dE\,(\Psi^\dagger_{E,r}\Psi_{E,r} - \psi^\dagger_{E,r}\psi_{E,r}) \\ &= \frac{1}{2}\int_{-\infty}^{\infty} dE\,(\Psi^\dagger_{E,r}\Psi_{E,r} - \psi^\dagger_{E,r}\psi_{E,r}) \\ &= -\frac{1}{2}\Psi^\dagger_{0,r}\Psi_{0,r}\,, \end{aligned} \tag{2.2}$$

with $\Psi_{E,r}$ ($\psi_{E,r}$) the eigenstates of the spectrum with energy E at position $\vec{r}$ when there is (is not) a defect, and $\int_{-\infty}^{\infty} dE$ excludes the zero energy state. In the last two steps, the completeness of the eigenstates is used:

$$\begin{aligned}\delta_{r-r'} &= \int_{-\infty}^{\infty} dE(\psi^\dagger_{E,r}\psi_{E,r'}) \\ &= \int_{-\infty}^{\infty} dE(\Psi^\dagger_{E,r}\Psi_{E,r'}) + \Psi^\dagger_{0,r}\Psi_{0,r'}\,. \end{aligned} \tag{2.3}$$

In general, to create a gap in graphene, terms $m_j\,M_j$ are added to the Hamiltonian H_0 where m_j are masses and M_j are the mass matrices which anticommute with H_0. If $M_j^2 = I$ and M_j anticommute with each other such as $H_{012} = H_0 + m_1M_1 + m_2M_2$, the square of the Hamiltonian has a simple form.

$$H^2_{012} = H_0^2 + m_1^2M_1^2 + m_2^2M_2^2\,. \tag{2.4}$$

Since $H_0^2 = |\vec{p}|^2$, the energy dispersion is $E = \pm\sqrt{|\vec{p}|^2 + m_1^2 + m_2^2}$. Hence, there is a gap of size $2\sqrt{m_1^2 + m_2^2}$ at the Dirac points.

2.2 Staggered Chemical Potential

If the on-site energy of electrons on site 2 is $2\,m_1$ larger than on site 1 where m_1 is a constant, the Hamiltonian becomes:

$$H_{01} = \sum_{r\in\Lambda_1}\left[-m_1c^\dagger_{1,r}c_{1,r} + m_1c^\dagger_{2,r+s_1}c_{2,r+s_1} - \sum_{i=1}^{3} t\,(c^\dagger_{1,r}c_{2,r+s_i} + h.c.)\right]. \tag{2.5}$$

Taking the Fourier transform of the Hamiltonian, $H_{01} = \sum_k \Psi^\dagger_k\,H^{(01)}_k\Psi_k$ where

$$H^{(01)}_k = \begin{pmatrix} -m_1 & -t\Phi_k \\ -t\Phi^*_k & m_1 \end{pmatrix}. \tag{2.6}$$

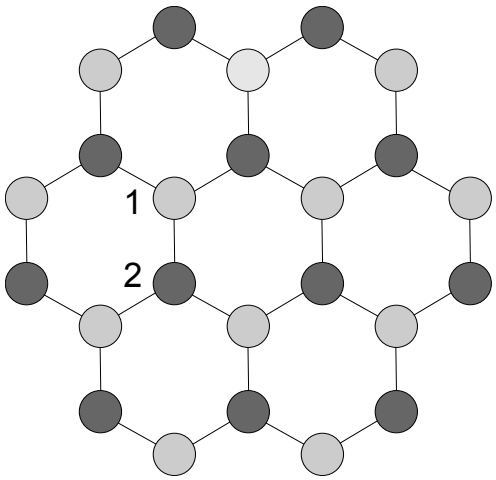

Figure 2.1: Graphene with a staggered chemical potential represented by adding $m_1 M_1$ to the Hamiltonian where m_1 is a constant. If $m_1 > 0$ is a positive constant, site 1 (light) is favoured, while site 2 (dark) is preferred for $m_1 < 0$.

Expanding around the Dirac points, $H_{01} = \int d^2\vec{x}\, \Psi^\dagger H^{(01)} \Psi$ where

$$\begin{aligned} H^{(01)} &= \begin{pmatrix} m_1 & i\partial_x - \partial_y & 0 & 0 \\ i\partial_x + \partial_y & -m_1 & 0 & 0 \\ 0 & 0 & m_1 & -i\partial_x - \partial_y \\ 0 & 0 & -i\partial_x + \partial_y & -m_1 \end{pmatrix} \\ &= -\gamma_0\gamma_1\partial_x - \gamma_0\gamma_2\partial_y + m_1 M_1 \,. \end{aligned} \tag{2.7}$$

A staggered chemical potential creates a density difference between the two sublattices, and m_1 is an order parameter for this charge density wave (CDW) [49]. Since M_2 and M_3 anticommute with the Hamiltonian, the energy spectrum must be symmetric about zero energy, and $E_p = \pm\sqrt{|\vec{p}|^2 + m_1^2}$. Therefore, at each Dirac point, a gap of $2m_1$ has been introduced. In addition, the time reversal operator T commutes with $H^{(01)}$.

Since $H^{(01)}\Psi = E\Psi$ does not couple the two Dirac points, two second-order differential equations arise:

$$(-\partial_x^2 - \partial_y^2)\, c_{2\pm} = (E^2 - m_1^2)\, c_{2\pm} \,. \tag{2.8}$$

For a given E, the solutions are:

$$\Psi_{1-} = \begin{pmatrix} e^{ip_x x}\, e^{ip_y y} \\ \frac{(-p_x+ip_y)}{E+m_1}\, e^{ip_x x}\, e^{ip_y y} \\ 0 \\ 0 \end{pmatrix},\ \Psi_{1+} = \begin{pmatrix} 0 \\ 0 \\ e^{-ip_x x}\, e^{-ip_y y} \\ \frac{(-p_x-ip_y)}{E+m_1}\, e^{-ip_x x}\, e^{-ip_y y} \end{pmatrix},$$

$$\Psi_{2-} = \begin{pmatrix} e^{ip_x x}\, e^{-ip_y y} \\ \frac{(-p_x-ip_y)}{E+m_1}\, e^{ip_x x}\, e^{-ip_y y} \\ 0 \\ 0 \end{pmatrix},\ \Psi_{2+} = \begin{pmatrix} 0 \\ 0 \\ e^{-ip_x x}\, e^{ip_y y} \\ \frac{(-p_x+ip_y)}{E+m_1}\, e^{-ip_x x}\, e^{ip_y y} \end{pmatrix},$$

$$\Psi_{3-} = \begin{pmatrix} e^{-ip_x x}\, e^{ip_y y} \\ \frac{(p_x+ip_y)}{E+m_1}\, e^{-ip_x x}\, e^{ip_y y} \\ 0 \\ 0 \end{pmatrix},\ \Psi_{3+} = \begin{pmatrix} 0 \\ 0 \\ e^{ip_x x}\, e^{-ip_y y} \\ \frac{(p_x-ip_y)}{E+m_1}\, e^{ip_x x}\, e^{-ip_y y} \end{pmatrix},$$

$$\Psi_{4-} = \begin{pmatrix} e^{-ip_x x}\, e^{-ip_y y} \\ \frac{(-p_x-ip_y)}{E+m_1}\, e^{-ip_x x}\, e^{-ip_y y} \\ 0 \\ 0 \end{pmatrix},\ \Psi_{4+} = \begin{pmatrix} 0 \\ 0 \\ e^{ip_x x}\, e^{ip_y y} \\ \frac{(-p_x+ip_y)}{E+m_1}\, e^{ip_x x}\, e^{ip_y y} \end{pmatrix}. \tag{2.9}$$

It is not surprising that the solutions are the same as those for H_0 except E is replaced with $E + m_1$. Hence, the solutions can still be related by the time reversal operator:

$$\Psi_{j\pm} = T\Psi_{j\mp}\,. \tag{2.10}$$

2.3 Domain Wall

A domain wall has a line defect which allows one site to be favoured to the left of the line, while the other site is preferred to the right of the line. For example, $m_1 = \tanh(y)$ has a line defect at $y = 0$ as illustrated in Fig. 2.2. A domain wall in a one dimensional Dirac system was first solved by Jackiw and Rebbi [27] showing charge fractionalization. In graphene, the Hamiltonian with a domain wall is similar to the case of a staggered chemical potential (2.7) with the exception that m_1 is now position dependent. Therefore, the Hamiltonian still anticommutes with M_2 and M_3 and commutes with T.

(a)

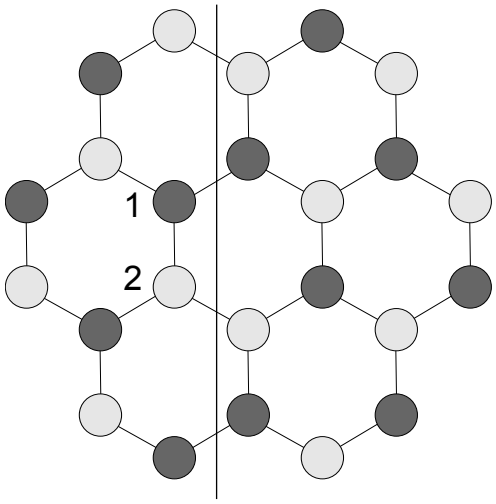

(b)

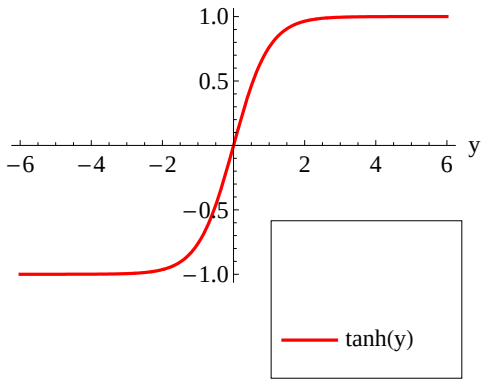

Figure 2.2: Line defect in graphene at $y = 0$. For $m_1 = \tanh(y)$, light sites have lower energy than the dark sites. To the left of the line ($y < 0$), site 2 has lower energy, while site 1 has lower energy to the right of the line ($y > 0$).

For a position dependent m_1, the second-order differential equations are:

$$\begin{aligned} E^{(-)}c_{2\pm} &= \frac{1}{E^{(+)}}\left(-\partial_x^2-\partial_y^2\right)\, c_{2\pm} \\ &\quad + \left[\mp i\partial_x\left(\frac{1}{E^{(+)}}\right) - \partial_y\left(\frac{1}{E^{(+)}}\right)\right]\left(\mp i\partial_x c_{2\pm} + \partial_y c_{2\pm}\right)\,, \end{aligned} \tag{2.11}$$

where $E^{(\pm)} = E \pm m_1$. In general, the equation with any analytic position dependent m_1 can be solved. For example, when $m_1 = \tanh(y)$, separation of variables is used where $\Psi_\pm = XY_\pm$ with X being a linear combination of $e^{ip_x x}$ and $e^{-ip_x x}$. $Y_\pm$ then satisfies:

$$\begin{aligned} E^{(+)}\partial_y^2 Y_\pm &= \left(\pm p_x \operatorname{sech}^2(y) - E^{(+)}\right)\left[E^2 - p_x^2 - \tanh^2(y)\right]\, Y_\pm \\ &\quad + \operatorname{sech}^2(y)\,\partial_y Y_\pm\,. \end{aligned} \tag{2.12}$$

To solve the differential equations in this thesis, the following method is used. $Y_\pm$ is expanded in polynomials around $y = 0$. In other words, $Y_\pm = \sum_{n=0}^{\infty} a_{n\pm}\, y^n$ with coefficients $a_{n\pm}$. Values are then calculated from the polynomials near $y = 0$ and used as initial conditions for finite difference methods such as Runge-Kutta to get $Y_\pm$ for larger y. Second-order differential equations in one variable have two linearly independent solutions. Near $y = 0$,

$$Y_{0\pm} = 1 + \frac{-E^3 \pm p_x + Ep_x^2}{2E}y^2 + \frac{-E^2 + p_x^2}{6E}y^3 + O(y^4)\,, \tag{2.13}$$

$$Y_{1\pm} = y + \frac{1}{2E}y^2 + \frac{-E^3 \pm p_x + Ep_x^2}{6E}y^3 + O(y^4)\,. \tag{2.14}$$

An example of the typical behaviour of $Y_\pm$ for $|p_x| < \sqrt{E^2 - m_1^2}$ is shown in Fig. 2.3. As $y \to \pm\infty$, $Y_\pm$ approaches the linearly independent solutions for a staggered chemical potential: $e^{ip_y y}$ and $e^{-ip_y y}$. Since $m_1^2 \to 1$ in this limit, the wavelength in y, $2\pi/p_y$, can be found analytically since $p_y = \pm\sqrt{E^2 - m_1^2 - p_x^2}$.

Examining the amplitude at $y = 0$, for $E > 1$, $Y_\pm$ changes from low amplitude to high amplitude, and for $E < 1$, $Y_\pm$ goes from high amplitude to low. This cannot be explained by the limits at infinity since $Y_\pm$ with a constant amplitude would be a possible solution. Hence, the amplitude change is linked to the function chosen to represent the line defect. Finding $c_{1\pm}$ from $c_{2\pm}$, the opposite behaviour is seen where the y-component changes from low amplitude to high amplitude for $E < 1$ and high to low for $E > 1$. For $|p_x| \geq \sqrt{E^2 - m_1^2}$, $Y_\pm$ decays exponentially as $y \to \pm\infty$. In particular, for a given E, when $\pm p_x = E$, it can be seen that $Y_\pm = \operatorname{sech}(y)$. The spinors are time reversal pairs: on one Dirac point, $p_x = E$,

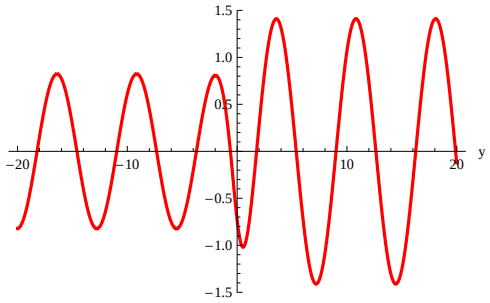

Figure 2.3: An example of $Y_\pm$ for $m_1 = \tanh(y)$ with $|p_x| < \sqrt{E^2 - m_1^2}$. Far from the defect, the wavelength in y is the same as the case of a staggered chemical potential: $2\pi/p_y$ where $p_y = \pm\sqrt{E^2 - m_1^2 - p_x^2}$. Near the defect, the amplitude changes. In this figure, $E = 2$, $p_x = 1.5$ with $X = e^{ip_x x}$. Therefore, the wavelength in y far from the origin is 7.25.

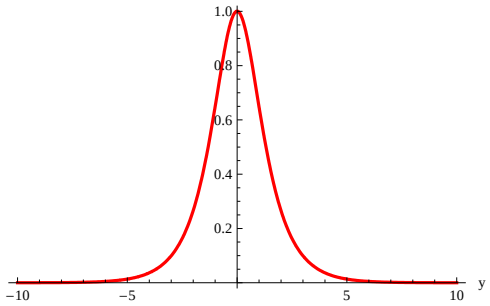

Figure 2.4: For the line defect with $m_1 = \tanh(y)$, $Y_\pm = \mathrm{sech}(y)$ when $\pm p_x = E$.

while on the other, $-p_x = E$:

$$\Psi_- = \begin{pmatrix} \mathrm{sech}(y)\, e^{iEx} \\ -\mathrm{sech}(y)\, e^{iEx} \\ 0 \\ 0 \end{pmatrix}, \quad \Psi_+ = \begin{pmatrix} 0 \\ 0 \\ \mathrm{sech}(y)\, e^{-iEx} \\ -\mathrm{sech}(y)\, e^{-iEx} \end{pmatrix}. \tag{2.15}$$

Therefore, there are $E = 0$ solutions bound in y.

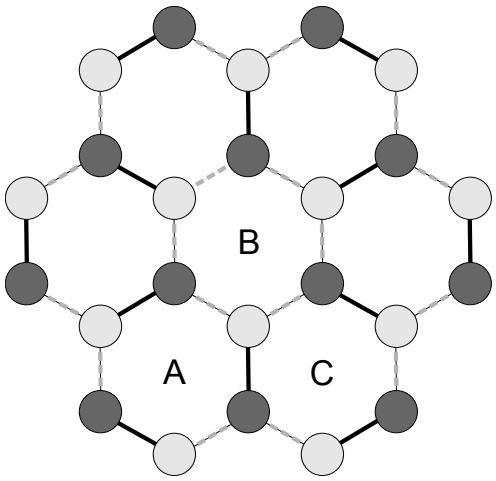

Figure 2.5: Kekulé Pattern with $\delta t_{r,r+s_i} = \Delta e^{i\vec{k}^+\cdot\vec{s}_i} e^{i\vec{G}\cdot\vec{r}}/3 + c.c.$. The solid dark (dashed light) lines indicate hopping is increased (decreased) by $2\Delta/3$ ($\Delta/3$). A, B, C indicate a possible choice of the unit cell.

2.4 Kekulé Pattern

Kekulé patterns can be created by modifying the hopping on the graphene lattice by adding a perturbation $\delta t_{r,r+s_i}$ to t:

$$H_{023} = -\sum_{r\in\Lambda_1}\left[\sum_{i=1}^{3}(t+\delta t_{r,r+s_i})\, c^{\dagger}_{1,r}c_{2,r+s_i} + h.c.\right]. \tag{2.16}$$

For $\delta t_{r,r+s_i} = \Delta e^{i\vec{k}^+\cdot\vec{s}_i} e^{i\vec{G}\cdot\vec{r}}/3 + c.c.$ where $\vec{G} = (\vec{k}^+ - \vec{k}^-)$ and Δ is a constant, the Fourier transform of this perturbed Hamiltonian results in coupling between the Dirac points on different lattice sites. The Hamiltonian is no longer invariant under translations by primitive lattice vectors. The bonds between $\sum_j n_j\vec{a}_j$ and $\sum_j n_j\vec{a}_{j+\vec{s}_i}$ are modified by $2\Delta\cos[-2\pi(\sum_j n_j)/3 + \vec{k}^+\cdot\vec{s}_i]/3$ where $\vec{k}^+\cdot\vec{s}_j = (0, 2\pi/3, -2\pi/3)$. The unit cell is now three times larger, and the resulting Kekulé hopping pattern showing is shown in Fig. 2.5.

Therefore, in the position basis after taking the Fourier transform and linearizing around

the Dirac points, the Hamiltonian is $H_{023} = \int d^2\vec{x}\, \Psi^\dagger H^{(023)} \Psi$ where

$$\begin{aligned} H^{(023)} &= \begin{pmatrix} 0 & i\partial_x - \partial_y & 0 & \Delta^* \\ i\partial_x + \partial_y & 0 & \Delta^* & 0 \\ 0 & \Delta & 0 & -i\partial_x - \partial_y \\ \Delta & 0 & -i\partial_x + \partial_y & 0 \end{pmatrix} \\ &= -\gamma_0\gamma_1\partial_x - \gamma_0\gamma_2\partial_y + \Delta M_2 + \Delta M_3\,. \end{aligned} \tag{2.17}$$

Since M_1 anticommutes with $H^{(023)}$, the spectrum is symmetric about zero energy, and energy spectrum has a gap of $2\,\Delta$ at each Dirac point: $E^{(023)} = \pm\sqrt{|\vec{p}|^2 + \Delta^2}$. Also, the time reversal operator commutes with $H^{(023)}$.

2.5 Kekulé Pattern: r-independent Vortices

Hou, Chamon, and Mudry [25] realized that a vortex in the Kekulé bond density wave (KBDW) order can lead to charge fractionalization. In this situation, the electric charge is conserved. Furthermore, the spectrum is symmetric about zero energy, is gapped, and has zero energy states. The vortex is represented by setting $\Delta = \Delta_0 e^{ip\,\theta}/2$ where $e^{ip\,\theta}$ represents a vortex with integer vorticity p and Δ_0 is a positive real number. The Hamiltonian $H^{(023)}$ can be rewritten in terms of r and θ:

$$H^{(023)} = \begin{pmatrix} 0 & i\partial_z & 0 & \Delta^* \\ i\partial_{z^*} & 0 & \Delta^* & 0 \\ 0 & \Delta & 0 & -i\partial_{z^*} \\ \Delta & 0 & -i\partial_z & 0 \end{pmatrix}, \tag{2.18}$$

where $\partial_z = \partial_x + i\partial_y = e^{i\theta}(\partial_r + \frac{i}{r}\partial_\theta)$ and $\partial_{z^*} = \partial_x - i\partial_y$. The components of the spinor are expanded in terms of complex exponentials:

$$\begin{pmatrix} c_{2-} \\ c_{1-} \\ c_{2+} \\ c_{1+} \end{pmatrix} = \sum_{n=-\infty}^{\infty} \begin{pmatrix} a_n\, e^{in\theta}\, e^{i\pi/4} \\ b_{n-1}\, e^{i(n-1)\,\theta}\, e^{-i\pi/4} \\ -c_{n+p-1}\, e^{i(n+p-1)\,\theta}\, e^{-i\pi/4} \\ d_{n+p}\, e^{i(n+p)\,\theta}\, e^{i\pi/4} \end{pmatrix}, \tag{2.19}$$

and $(a_n, b_{n-1}, c_{n+p-1}, d_{n+p})$ are real and depend only on r. The subscripts match the phase they multiply. There are now four coupled differential equations:

$$\begin{aligned} -E\, a_n + [\partial_r - (n-1)/r]\, b_{n-1} + \Delta_0\, d_{n+p} &= 0\,, \\ (\partial_r + n/r)\, a_n + E\, b_{n-1} + \Delta_0\, c_{n+p-1} &= 0\,, \\ \Delta_0\, b_{n-1} + E\, c_{n+p-1} + [\partial_r + (n+p)/r]\, d_{n+p} &= 0\,, \\ \Delta_0\, a_n + [\partial_r - (n+p-1)/r]\, c_{n+p-1} - E\, d_{n+p} &= 0\,. \end{aligned} \tag{2.20}$$

In the definition of the spinor components, the $\pm\pi/4$ phase factors are chosen such that the number of equations is reduced to four from eight since the real and imaginary parts of $(a_n, b_{n-1}, c_{n+p-1}, d_{n+p})$ satisfy the same differential equations. Equally important, at most four radial components (a_n, b_{n-1}, c_{n+p-1}, d_{n+p}) are coupled for a given n. The differential equations are examined for bound state solutions. For zero energy, there are two pairs of coupled first-order differential equations which can be decoupled into two second-order differential equations:

$$-r^2\partial_r^2 d - (1+p)\, r\partial_r d + (n^2 + np + r^2\Delta_0^2)\, d = 0\,, \tag{2.21}$$

$$-r^2\partial_r^2 c + (-1+p)\, r\partial_r c + [(1-n)(1-n-p) + r^2\Delta_0^2]\, c = 0\,, \tag{2.22}$$

where $c = c_{n+p-1}$ and $d = d_{n+p}$. The coefficients $a = a_n$ and $b = b_{n-1}$ can then be determined from c and d. The solutions of the differential equations are expanded in polynomials. Near $r = 0$, c goes as r^{1-n} and r^{-1+n+p}. For c to be normalizable at $r = 0$, the smallest integer power must be greater than or equal to zero. Values near $r = 0$ are calculated from the polynomials and used as initial conditions for finite difference methods for larger r. The superposition of the two linearly independent solutions which is normalizable as $r \to \infty$ is then found. Since a, which goes as $(n+p-1)\, c/r$ near $r = 0$, must also be normalizable, the smallest power of c must actually be greater than or equal to 1, or $n = -p + 1$. Therefore, the solutions are $0 \geq n \geq 2 - p$ or $n = -p + 1$. For example, for $p = 1$, $n = 0$, and the zero energy solution can be found analytically as well:

$$\Psi = \begin{pmatrix} e^{-\Delta_0 r} \\ 0 \\ e^{-\Delta_0 r} \\ 0 \end{pmatrix}. \tag{2.23}$$

For $p = 2$, n can be 0 or -1. So for a given $p > 0$, there are p zero energy bound state solutions on site 2 for $0 \geq n \geq 1 - p$. Comparing the equations for (a, c) and (b, d), they

$\|p\|$	$E_{p,1}$	$E_{p,3}$	$E_{p,5}$	$E_{p,7}$	$E_{p,9}$
1	0	0.943	0.980	0.990	0.994
2	0	0.867	0.943	0.968	0.980
3	0	0.800	0.904	0.943	0.962
4	0	0.745	0.866	0.917	0.943
5	0	0.700	0.831	0.891	0.923
6	0	0.661	0.800	0.866	0.904

Table 2.1: $E_{p,l} = \mathrm{sgn}(l)\sqrt{1-[p/(|l|+|p|-1)]^2}$ with degeneracy $|l|+|p|-1$ are the bound state energies for $\Delta_0 = 1$. Higher vorticity leads to bound state energies closer to zero.

are identical after mapping $p \to -p$ and $n \to 1-n$. Hence, for $p < 0$, there are p bound state zero energy solutions on site 1 for $1 \le n \le -p$. For example, for $p = -1$, $n = 1$, and for $p = 2$, n can be 1 or 2. As a result, when $|p| = 1$, there is a single zero energy state, and fractional charge is found. When the zero energy state is not filled, the charge is $-1/2$, and when the zero energy state is filled, the charge is $1/2$. The single zero energy solution is protected since the spectrum must be symmetric. This does not hold when there is an even number of zero modes.

To solve for the non-zero bound state energies, the four coupled first-order differential equations are decoupled into a single fourth-order differential equation:

$$\begin{aligned} -r^4\partial_r^4 a \;=\;& 4r^3\partial_r^3 a - r^2[-1+2j^2+2j(-1+p)-2p+p^2]\partial_r^2 a \\ &+r^4(-2\Delta^2+2E^2)\partial_r^2 a - r[1+2j(-1+p)-2p+p^2]\partial_r a \\ &+r^3(-4+4E^2)\partial_r a + j^2[-6p+p^2-2(-1+E^2)r^2]\,a \\ &+r^2[2(-1+E^2)p - E^2p^2 + (-1+E^2)^2r^2)]\,a \\ &+[j^4+2j^3(-1+p)-2(-1+E^2)j(-1+p)r^2]\,a\,. \end{aligned} \tag{2.24}$$

The fourth-order differential equation can be solved in the same manner as the second-order differential equations. For any p, an infinite number of bound states is numerically found at:

$$E_{p,l} = \mathrm{sgn}(l)\,\Delta_0\sqrt{1-[p/(|l|+|p|-1)]^2}\,, \tag{2.25}$$

with degeneracy $|l|+|p|-1$ where l is an odd integer. Table 2.1 shows the bound state energies get closer to zero with increasing p. An example of energies with their degeneracies for $p = 1, 2$ is shown in Tables 2.2 and 2.3.

l \ n	−2	−1	0	1	2
−5	−0.980	−0.980	−0.980	−0.980	−0.980
−3		−0.943	−0.943	−0.943	
∓1			0		
3		0.943	0.943	0.943	
5	0.980	0.980	0.980	0.980	0.980

Table 2.2: $E_{1,l} = \mathrm{sgn}(l)\sqrt{1 - 1/l^2}$ with degeneracy $|l|$ for odd integers l are the bound state energies for $\Delta_0 = 1$ for $p = 1$.

l \ n	−3	−2	−1	0	1	2
−5	−0.943	−0.943	−0.943	−0.943	−0.943	−0.943
−3		−0.867	−0.867	−0.867	−0.867	
∓1			0	0		
3		0.867	0.867	0.867	0.867	
5	0.943	0.943	0.943	0.943	0.943	0.943

Table 2.3: $E_{2,l} = \mathrm{sgn}(l)\sqrt{1 - [2/(|l| + 1)]^2}$ with degeneracy $|l| + 1$ are the bound state energies for $\Delta_0 = 1$ for $p = 2$.

To differentiate between degenerate energies, $\Psi_{p,l,n}$ is written with three indices. In this notation, the zero energy solution for $p = 1$ is:

$$\Psi_{1,1,0} = \begin{pmatrix} e^{-\Delta_0 r}\, e^{i\pi/4} \\ 0 \\ e^{-\Delta_0 r}\, e^{-i\pi/4} \\ 0 \end{pmatrix}, \tag{2.26}$$

and the radial components for $\Psi_{p,l,n}$ with different p and l are shown in Fig. 2.6 and 2.7. For a given n, when $|l|$ is increased, both the number of nodes for each of the radial components and their spread in r increase as seen in Fig. 2.8. $\Psi_{p,l,n}$ with larger n oscillate more in θ. For odd p, there are time reversal pairs such that $\Psi_{p,l,-n} = T\Psi_{p,l,n}$, and therefore, for $n = 0$, $\Psi_{p,l,0} = T\Psi_{p,l,0}$, the time reversal operator transforms this spinor into itself. For even p, spinors Ψ_{p,l,n_1} and Ψ_{p,l,n_2} are time reversal pairs if $-n_1 + 1/2 = n_2 - 1/2$ for $n_1 < n_2$. The positive and negative energy solutions are related: $\Psi_{p,-l,b} = M_1\Psi_{p,l,n}$. Also, solutions for p can be mapped to $-p$: $\Psi_{-p,l,1-n} = -i\gamma_1 K\Psi_{p,l,n}$.

2.6 Kekulé Pattern: r-dependent Vortices

The Hamiltonian for r-dependent vortices is the same as the r-independent situation with the exception that Δ_0 now depends on r. Therefore, the matrices that anticommute and commute with the Hamiltonian are already known. Fractional charge is found when the spectrum is half filled with the zero-energy state unoccupied $(-1/2)$ or occupied $(1/2)$ [25]. The case $\Delta_0 = r$ is closely examined. The zero energy solutions are found by restating the coupled first-order differential equations into two second-order differential equations:

$$-r^2\partial_r^2 c + pr\partial_r c + [2 + n^2 + n(-3 + p) - 2p + r^4]\, c = 0\,, \tag{2.27}$$

$$-r^2\partial_r^2 d - pr\partial_r d + (n + n^2 + p + np + r^4)\, d = 0\,. \tag{2.28}$$

Near $r = 0$, c goes as r^{2-n} and r^{-1+n+p}. Since a goes as $(n+p-1)\, c/r^2$, the smallest power needs to be greater than or equal to 1 or $n = -p+1$. Therefore, the number of zero energy solutions are identical to the r-independent case: $0 \geq n \geq 1 - p$. For a given $p > 0$, there are p zero energy solutions on site 2. Also, the mapping from (b, d) to (a, c) where $p \to -p$ and $n \to 1 - n$ still holds. Hence, for $p < 0$, there are p zero energy solutions on site 1 for

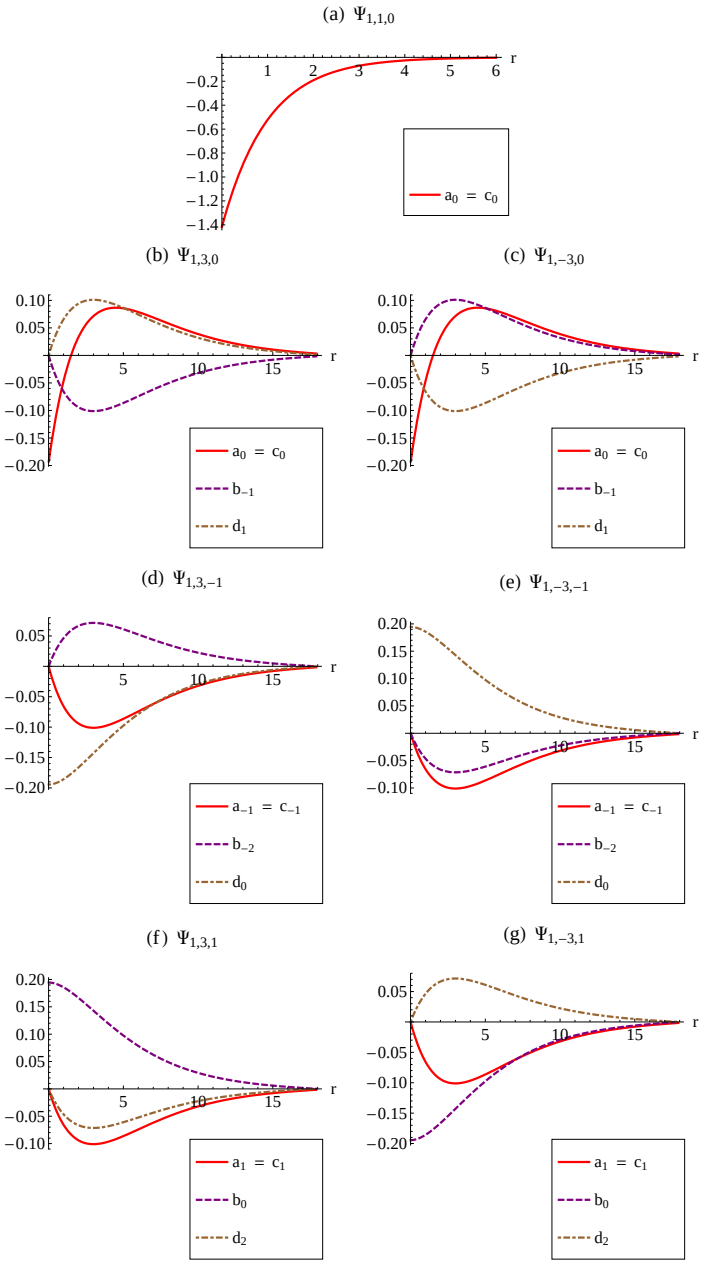

Figure 2.6: Radial components of $\Psi_{1,l,n}$ for a single vortex ($p = 1$) with $\Delta_0 = 1$. There is one zero energy state (a). The next higher energy state is a triplet: 0.943 (b,d,f); the lower energy state is also a triplet: -0.943 (c,e,g). $\Psi_{1,l,0}$ (a,b,c) transform into themselves through time reversal. The time reversal pairs are $\Psi_{1,l,n}$ and $\Psi_{1,l,-n}$: (d,f) and (e,g).

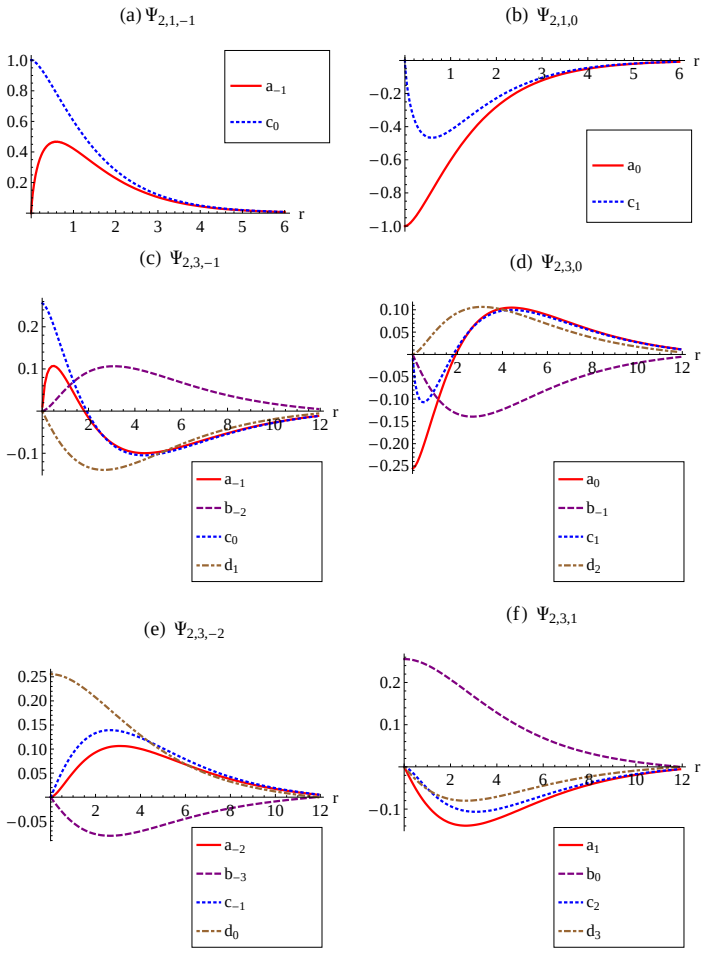

Figure 2.7: Radial components of $\Psi_{2,l,n}$ for $p = 2$ with $\Delta_0 = 1$. There are two zero energy solutions: (a,b). The next higher state, 0.867, has four solutions: (c,d,e,f). The time reversal pairs for the above states are Ψ_{2,l,n_1} and Ψ_{2,l,n_2} where $-n_1 + 1/2 = n_2 - 1/2$ for $n_1 < n_2$: (a,b), (c,d), and (e,f).

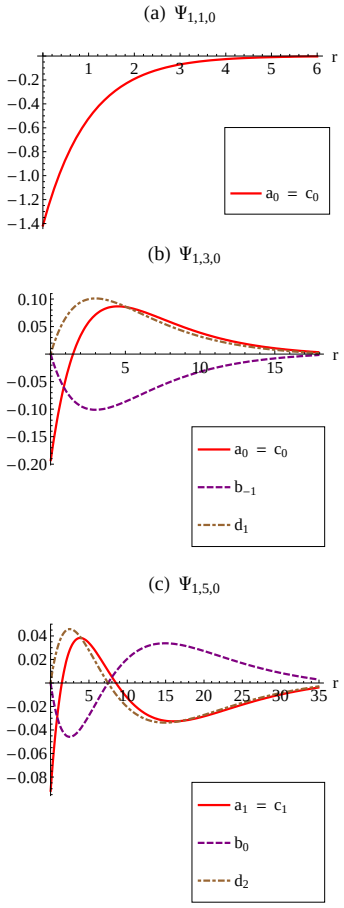

Figure 2.8: Radial components of $\Psi_{1,l,0}$ for a single vortex ($p = 1$) with $\Delta_0 = 1$ and $n = 0$. For a given n, each time $|l|$ is increased by j, the number of nodes for each of the radial components also increase by j. Also, their spread in r increases with $|l|$.

$1 \leq n \leq -p$. For all p, the differential equations for zero energy have the following form that can be solved exactly with Bessel functions:

$$r^2\partial_r^2 f + C_1 r\partial_r f + (C_2 r^n + C_3) f = 0\,, \tag{2.29}$$

with constants C_j.

The four coupled first-order differential equations are decoupled into a single fourth-order differential equation to solve for the non-zero bound state energies.

$$\begin{aligned} r^4\partial_r^4 a \;=\; & -2r^3\partial_r^3 a + 2r^4\partial_r^2 a - 2E^2 r^2\partial_r^2 a \\ & +(2 - 2j + 2j^2 - 2p + 2jp + p^2)\partial_r^2 a + 6r^5\partial_r a - 2E^2 r^3\partial_r a \\ & +(2j - 2j^2 - 2p + 2jp + p^2)\, r\partial_r a - r^8 a + 2E^2 r^6 a \\ & +(4 - E^4 + 2j - 2j^2 + 4p - 2jp)\, r^4 a \\ & +(E^2 - 2E^2 j + 2E^2 j^2 - 2E^2 p + 2E^2 jp + E^2 p^2)\, r^2 a \\ & +(3j^2 + 2j^3 - j^4 + 2j^2 p - 2j^3 p - j^2 p^2)\, a\,. \end{aligned} \tag{2.30}$$

For $|p| = 1$ with $\Delta_0 = r$, an infinite number of bound states are numerically found at $E_l = \mathrm{sgn}(l)\sqrt{2|l|}$ where l is an integer. For zero energy, $l = 0$, the degeneracy is p which is the same as the r-independent case, but for $l \neq 0$, the degeneracy is $2|l|$ as seen in Table 2.4. Unlike the case of r-independent vortex, there can be double degeneracy for certain l and p. Therefore, p, l, n do not uniquely define a spinor. This degeneracy can be broken by defining two patterns: one without the extra degeneracy (Table 2.5) and one with only the extra degeneracy (Table 2.6). The first pattern has $E_l = \mathrm{sgn}(l)\sqrt{2|l|}$ with degeneracy $|l| + 1$ for integer l, while the second pattern has $E_l = \mathrm{sgn}(l)\sqrt{2|l|}$ with degeneracy $|l| - 1$ for integer $|l| \geq 2$. The solutions to the second pattern have the same θ dependence as a solution in the first pattern, but the number of nodes in the radial components are different. For higher p, the energy spectrum is a perturbation of the spectrum of the $|p| = 1$ case but with more copies of the $n = 0$ solutions. Unlike the $|p| = 1$ case, the highest degeneracy is two, but the energies are near those for $|p| = 1$ as shown in Tables 2.7 and 2.8.

Herbut and Lu [24] solved the $|p| = 1$ case analytically by rewriting the Hamiltonian in terms of fictitious bosonic and fermionic creation and annihilation operators:

$$H_p^{(h)} = \vec{\alpha}\cdot\vec{p} + \vec{\beta}\cdot\vec{r}, \tag{2.31}$$

where α_j and β_j are Dirac matrices satisfying:

$$\{\alpha_i, \alpha_j\} = \{\beta_i, \beta_j\} = 2\delta_{i,j}\,, \tag{2.32}$$

l \ n	−3	−2	−1	0	1	2	3
−3	−2.449		−2.449 (2)		−2.449 (2)		−2.449
−2		−2		−2 (2)		−2	
−1			−1.414		−1.414		
0				0			
1			1.414		1.414		
2		2		2 (2)		2	
3	2.449		2.449 (2)		2.449 (2)		−2.449

Table 2.4: The bound state energies for $\Delta_0 = r$ and $p = 1$ are $E_l = \mathrm{sgn}(l)\sqrt{2|l|}$. The degeneracy of the zero-energy state is 1, while all other levels have degeneracy $2|l|$. The parenthesis after the number indicates whether there is an extra degeneracy for a given n. Two patterns can be created: Tables 2.5 and 2.6.

l \ n	−3	−2	−1	0	1	2	3
−3	−2.449		−2.449		−2.449		−2.449
−2		−2		−2		−2	
−1			−1.414		−1.414		
0				0			
1			1.414		1.414		
2		2		2		2	
3	2.449		2.449		2.449		−2.449

Table 2.5: The first pattern of bound state energies for $\Delta_0 = r$ and $p = 1$ are $E_l = \mathrm{sgn}(l)\sqrt{2|l|}$ for integer l. The degeneracy of the levels in the first pattern are $|l| + 1$.

l \ n	−2	−1	0	1	2
−4	−2.828		−2.828		−2.828
−3		−2.449		−2.449	
−2			−2		
−1					
0					
1					
2			2		
3		2.449		2.449	
4	2.828		2.828		2.828

Table 2.6: The second pattern of bound state energies for $\Delta_0 = r$ and $p = 1$ are $E_l = \mathrm{sgn}(l)\sqrt{2|l|}$ for integer $|l| \geq 2$. The degeneracy of the levels in the second pattern are $|l| - 1$.

l \ n	−4	−3	−2	−1	0	1	2	3
−3	−2.424		−2.389			−2.389		−2.424
−2		−1.972		−1.901	−1.901		−1.972	
−1			−1.384			−1.384		
0				0	0			
1			1.384			1.384		
2		1.972		1.901	1.901		1.972	
3	2.424		2.389			2.389		2.424

Table 2.7: The first pattern of bound state energies for $\Delta_0 = r$ and $p = 2$. The $p = 2$ energies are small perturbations from the $p = 1$ solutions with the $n = 0$ becoming $n = 0, -1$ (Table 2.5).

l \ n	−3	−2	−1	0	1	2
−4	−3.208		−3.198	−3.198		−3.208
−3		−2.882			−2.882	
−2			−2.509	−2.509		
−1						
0						
1						
2			2.509	2.509		
3		2.882			2.882	
4	3.208		3.198	3.198		3.208

Table 2.8: The second pattern of bound state energies for $\Delta_0 = r$ and $p = 2$. The $p = 2$ energies are small perturbations from the $p = 1$ solutions with the $n = 0$ becoming $n = 0, -1$ (Table 2.6).

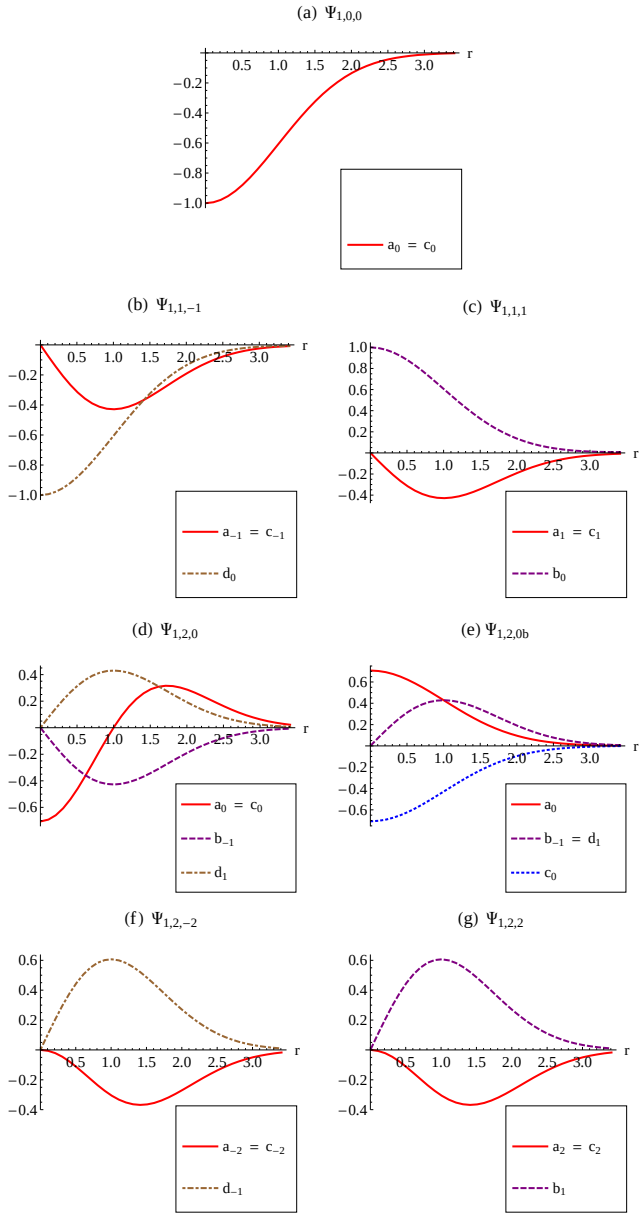

Figure 2.9: Radial components of $\Psi_{1,l,n}$ for a single vortex ($p = 1$) with $\Delta_0 = r$. There is one zero energy state (a). The next higher energy state is a time reversal pair: 1.414 (b,c). The next higher energy state has a degeneracy of four. Two are time reversal pairs (f,g), while the other two map to themselves with time reversal (d,e). The lowest energy state in magnitude for the second pattern is (e). It has the same θ dependence as (a), but orthogonal to it due to more nodes in r.

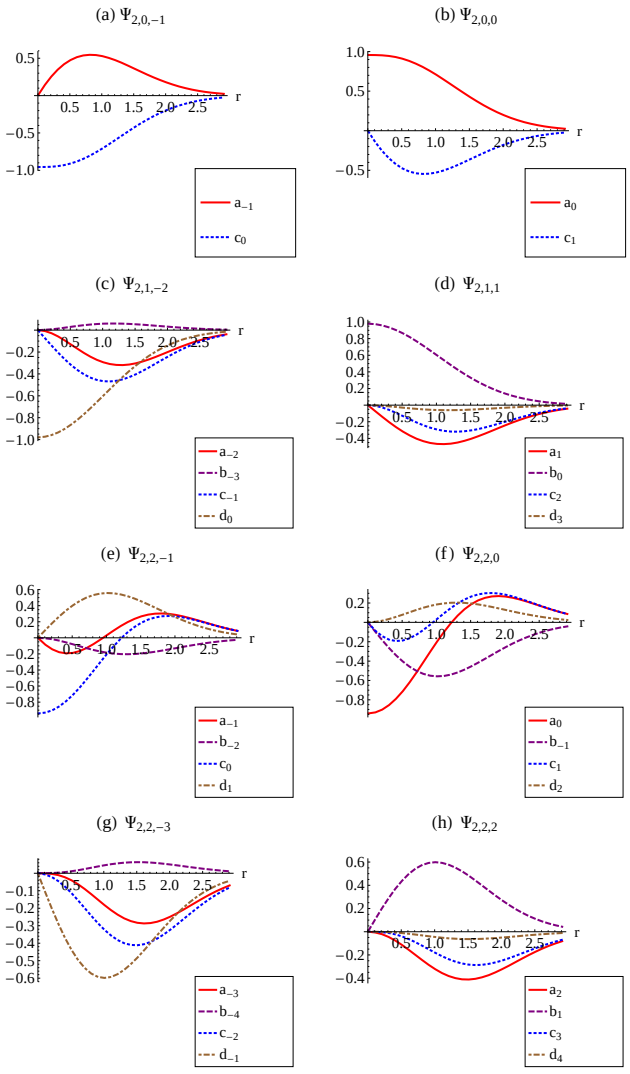

Figure 2.10: Radial components of $\Psi_{2,l,n}$ with $\Delta_0 = r$ and $p = 2$. The energy states are perturbations of the states of the $p = 1$ case. There are two zero energy states which are time reversal pairs (a,b). The next higher energy state is also a time reversal pair: 1.384 (c,d). The next higher energy which was four-fold degeneracy in $p = 1$ has been split into two time reversal pairs: 1.901 (e,f) and 1.972 (g,h).

and $\{\alpha_i, \beta_j\} = 0$.

$$\begin{aligned}(H_p^{(h)})^2 &= \vec{p}^{\,2} + r^2 + i\vec{\beta}\cdot\vec{\alpha} \\ &= 2\sum_{j=1}^{2}(b_j^\dagger b_j + a_j^\dagger a_j)\,, \end{aligned} \tag{2.33}$$

where b_j are bosonic operators defined by $b_j = r_j + ip_j$ and a_j are fermionic operators defined by $a_j = (\beta_j + i\alpha_j)/2$. Hence, the energy spectrum is $E = \pm\sqrt{2N}$ for an integer N for $N \geq 2$.

The number of states for each energy can be explained due to an accidental, or non-geometrical, degeneracy. Angular momentum-like vectors that commute with $(H_p^{(h)})^2$ can be defined:

$$L_i = \left(\sum_{\mu,\nu=1}^{2} b_\mu^\dagger \sigma_i^{\mu\nu} b_\nu\right)/2\,, \tag{2.34}$$

$$S_i = \left(\sum_{\mu,\nu=1}^{2} a_\mu^\dagger \sigma_i^{\mu\nu} a_\nu\right)/2\,. \tag{2.35}$$

By examining $\vec{L}^2$ and $\vec{S}^2$ with eigenvalues $l(l+1)$ and $s(s+1)$ respectively, the values of l and s are found:

$$l = N^b/2\,, \tag{2.36}$$

$$s = N^f(2 - N^f)/2\,, \tag{2.37}$$

where $N^b(N^f)$ is the number of bosons (fermions). Therefore, from $\vec{J} = \vec{S} + \vec{L}$ for $N \geq 2$,

$$j_\pm = l \pm s = (N - N^f \pm N^f(2 - N^f))/2\,, \tag{2.38}$$

has two values: $\{N/2,\, N/2 - 1\}$ since N^f can only be $\{0, 1\}$. As a result, there are:

$$2(j_+) + 1 + 2(j_-) + 1 = 2N\,, \tag{2.39}$$

degenerate energy eigenvalues.

In general, Δ_0 with any analytic r-dependence can be solved because the equations always decouple into a fourth-order differential equation. If Δ_0 goes as r near $r = 0$ and

l \ n	−2	−1	0	1	2
−5	−0.980	−0.980	−0.981	−0.980	−0.980
−3		−0.940	−0.945	−0.940	
∓1			0		
3		0.940	0.945	0.940	
5	0.980	0.980	0.981	0.980	0.980

Table 2.9: The bound state energies for $\{\Delta_0 = r \text{ for } r < 1\}$ and $\{\Delta_0 = 1 \text{ for } r \geq 1\}$ with $p = 1$ are shown. The bound state energies are perturbations of the energies from the $\Delta_0 = 1$ case (Table 2.2).

l \ n	−3	−2	−1	0	1	2	3
−3	−2.448		−2.448 (2)		−2.448 (2)		−2.448
−2		−2.000		−2.000 (2)		−2.000	
−1			−1.415		−1.415		
0				0			
1			1.415		1.415		
2		2.000		2.000 (2)		2.000	
3	2.448		2.448 (2)		2.448 (2)		−2.448

Table 2.10: The bound state energies for $\{\Delta_0 = r \text{ for } r < 3\}$ and $\{\Delta_0 = 3 \text{ for } r \geq 3\}$ with $p = 1$ are shown. The bound state energies are perturbations of the energies of the $\Delta_0 = r$ case (Table 2.4).

is constant as $r \to \infty$, $\{\Delta_0 = r \text{ for } r < \Delta_c\}$ and $\{\Delta_0 = \Delta_c \text{ for } r \geq \Delta_c\}$, the bound state energies is a mixture of the two cases. For small Δ_c with any p, the bound state energies are perturbations of the bound state energies for constant Δ_0 as seen in Table 2.9. On the other hand, for larger Δ_c with any p, the bound state energies are perturbations of the bound state energies for $\Delta_0 = r$ as seen in Table 2.10.

2.7 Non-zero CDW and KBDW Order Parameters

The case where both CDW and KBDW order parameters are non-zero is now examined. Chamon *et al.* [7] found that the value of the charge is dependent on the ratio of m_1/m_{123} where $m_{123} = \sqrt{m_1^2 + |\Delta|^2}$. From the Lagrangian, they computed the current, $j_\mu = \langle \psi \gamma_\mu \psi \rangle$, with respect to the order parameters $\vec{n} = (m_1, \Delta_0 \cos\theta, \Delta_0 \sin\theta)$ where m_1 and Δ_0 are

constant. The Lagrangian is:

$$\mathscr{L} = \psi^\dagger (i\gamma_0\gamma_\mu\partial_u - m_j M_j)\,\psi\,, \tag{2.40}$$

and the current operator is:

$$j^\mu = \frac{1}{8\pi}\,\epsilon^{\mu\nu\rho}\,\vec{n}\cdot(\partial_\nu\vec{n}\wedge\partial_\rho\vec{n})\,, \tag{2.41}$$

where ϵ is the Levi-Civita symbol. The charge Q is then found to be:

$$Q = \pm\frac{1}{2}\left(1 - \frac{|m_1/\Delta_0|}{\sqrt{1+m_1^2/\Delta_0^2}}\right)\,, \tag{2.42}$$

where $\pm$ depends on whether the zero energy state is unoccupied or occupied. When $m_1 = \Delta_0$, $Q = 1/4$. As expected, when $|m_1| \gg |\Delta_0|$, the charge is zero, and when $|m_1| \ll |\Delta_0|$, the charge is $\pm 1/2$. Repeating this process for r-dependent m_1 and Δ_0, Chamon *et al.* found that the value of the order parameters as r goes ∞ determines the charge.

The resulting Hamiltonian is $H_{0123} = \int d^2\vec{x}\,\Psi^\dagger H^{(0123)}\Psi$ where

$$\begin{aligned} H^{(0123)} &= \begin{pmatrix} m_1 & i\partial_x - \partial_y & 0 & \Delta^* \\ i\partial_x + \partial_y & -m_1 & \Delta^* & 0 \\ 0 & \Delta & m_1 & -i\partial_x - \partial_y \\ \Delta & 0 & -i\partial_x + \partial_y & -m_1 \end{pmatrix} \\ &= -i\gamma_0\gamma_1\partial_x - i\gamma_0\gamma_2\partial_y + m_1 M_1 + \Delta M_2 + \Delta M_3\,. \end{aligned} \tag{2.43}$$

The following coupled first-order differential equations appear:

$$\begin{aligned} (m_1 - E)\,a_n + [\partial_r - (n-1)/r]\,b_{n-1} + \Delta_0\,d_{n+p} &= 0\,, \\ (\partial_r + n/r)\,a_n + (m_1 + E)\,b_{n-1} + \Delta_0\,c_{n+p-1} &= 0\,, \\ \Delta_0\,b_{n-1} - (m_1 - E)\,c_{n+p-1} + [\partial_r + (n+p)/r]\,d_{n+p} &= 0\,, \\ \Delta_0\,a_n + [\partial_r - (n+p-1)/r]\,c_{n+p-1} - (m_1 + E)\,d_{n+p} &= 0\,, \end{aligned} \tag{2.44}$$

when the spinor is expanded in θ as previously:

$$\begin{pmatrix} c_{2-} \\ c_{1-} \\ c_{2+} \\ c_{1+} \end{pmatrix} = \sum_{n=-\infty}^{\infty} \begin{pmatrix} a_n\,e^{in\theta}\,e^{i\pi/4} \\ b_{n-1}\,e^{i(n-1)\theta}\,e^{-i\pi/4} \\ -c_{n+p-1}\,e^{i(n+p-1)\theta}\,e^{-i\pi/4} \\ d_{n+p}\,e^{i(n+p)\theta}\,e^{i\pi/4} \end{pmatrix}\,. \tag{2.45}$$

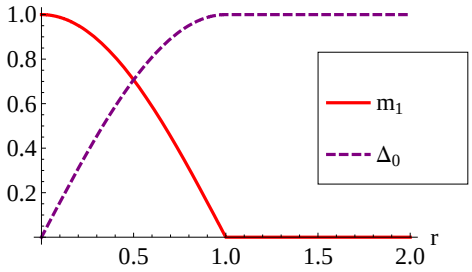

Figure 2.11: A meron changes m_1 from 1 to 0 while keeping $m_1^2 + \Delta_0^2$ constant. The bound state energies for $\{m_1 = \cos(\pi r/2)$ for $r < 1\}$ and $\{0$ for $r \geq 1\}$ are solved.

For any r-dependent order parameters: m_1 and Δ_0, the equations decouple into a fourth-order differential equation. Therefore, the bound state energies can be solved for any analytic order parameters. The bound state energies for a meron where $\{m_1 = \cos(\pi r/2)$ for $r < 1\}$ and $\{0$ for $r \geq 1\}$ while keeping $m_1^2 + \Delta_0^2$ constant as shown in Fig. 2.11 is solved. The bound state energy spectrum is no longer symmetric about zero energy and is a perturbation of the bound state energy spectrum of $m_1 = 0$ and $\Delta_0 = 1$ as shown in Table 2.11. This is not surprising since this configuration is similar to the case where $m_1 = 0$ with $\{\Delta_0 = r$ for $r < 1\}$ and $\{\Delta_0 = 1$ for $r \geq 1\}$ (which is a perturbation of spectrum from the $m_1 = 0$ and $\Delta_0 = 1$ case). Another situation where both CDW and KBDW order parameters are non-zero is the Skyrmion. For a Skyrmion, m_1 changes from 1 to -1 while keeping $m_1^2 + \Delta_0^2$ constant. An example is $\{m_1 = \cos(\pi r)$ for $r < 1\}$ and $\{-1$ for $r \geq 1\}$ as shown in Fig. 2.12.

2.8 Quantum Hall State

Haldane [19] revealed that $m_4 M_4$ represents directed next nearest neighbour hopping in the presence of fluxes with no net magnetic field. Furthermore, at half-filling, the state exhibits the quantum Hall effect (QHE). The quantized Hall conductivity is proportional to the Chern number n, which is the sum of the Chern numbers for each band n_m where for band m:

$$n_m = \frac{1}{2\pi} \int d^2\vec{p}\, F_m \,, \tag{2.46}$$

(a)

l \ n	−1	0	1
−3	−0.948	−0.940	−0.948
∓1		0.301	
3	0.930	0.950	0.930

(b)

l \ n	−2	−1	0	1
−3	−0.876	−0.859	−0.859	−0.876
∓1		0.175	0.175	
3	0.848	0.877	0.877	0.848

Table 2.11: The bound state energies for a meron: $\{m_1 = \cos(\pi r/2)$ for $r < 1\}$ and $\{0$ for $r \geq 1\}$ with (a) $p = 1$ and (b) $p = 2$. The bound state energies are perturbations of the energies from the $m_1 = 0$ and $\Delta_0 = 1$ case (Table 2.2 and Table 2.3).

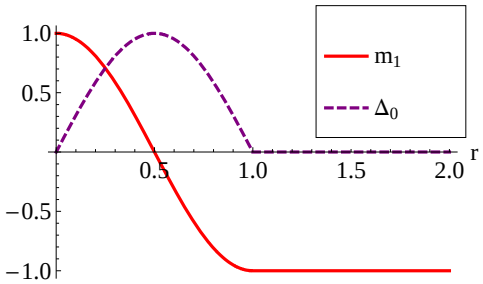

Figure 2.12: A Skyrmion changes m_1 from 1 to -1 while keeping $m_1^2 + \Delta_0^2$ constant. An example is $\{m_1 = \cos(\pi r)$ for $r < 1\}$ and $\{-1$ for $r \geq 1\}$.

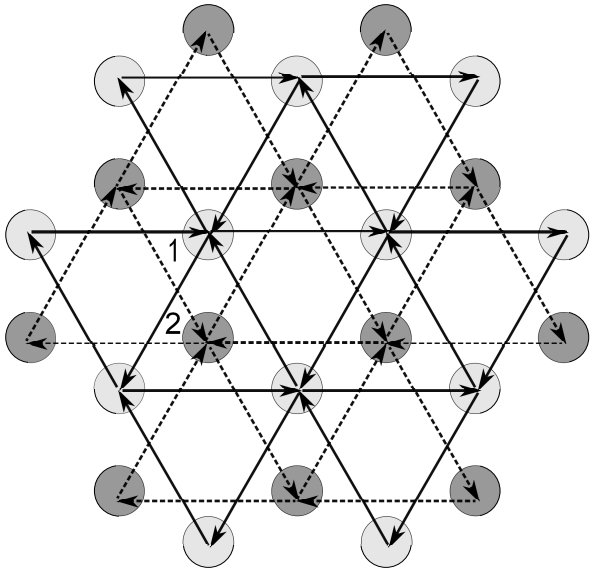

Figure 2.13: Graphene with directed NNN hopping exhibits the QHE. The energy spectrum has a gap in the bulk with topologically protected edge states. There are two currents: one between sites 1 (solid) and the other between sites 2 (dotted).

with the Berry flux defined by $F_m = \vec{\nabla} \times A_m$, $A_m = i\langle\psi_m|\vec{\nabla}_k|\psi_m\rangle$, and ψ_m is the wavefunction of a particular band. Even though this QHE state is insulating, there is a topologically protected edge state due to the different topological Chern numbers at the surface.

Expanding around the Dirac points, $H_{04} = \int d^2\vec{x}\,\Psi^\dagger H^{(04)}\Psi$ in the position basis where

$$\begin{aligned} H^{(04)} &= \begin{pmatrix} m_4 & i\partial_x - \partial_y & 0 & 0 \\ i\partial_x + \partial_y & -m_4 & 0 & 0 \\ 0 & 0 & -m_4 & -i\partial_x - \partial_y \\ 0 & 0 & -i\partial_x + \partial_y & m_4 \end{pmatrix} \\ &= -\gamma_0\gamma_1\partial_x - \gamma_0\gamma_2\partial_y + m_4 M_4\,. \end{aligned} \tag{2.47}$$

As expected, the energy dispersion is gapped: $E = \pm\sqrt{|\vec{p}|^2 + m_4^2}$, and there is no matrix that anticommutes with this Hamiltonian. Also, M_4 no longer commutes with the time reversal operator.

2.9 Non-zero CDW, KBDW, QHE Order Parameters

Considering the situation where all four order parameters are now non-zero, the resulting Hamiltonian is $H_{01234} = \int d^2\vec{x}\, \Psi^\dagger H^{(01234)} \Psi$ where

$$\begin{aligned} H^{(01234)} &= \begin{pmatrix} m_1+m_4 & i\partial_x - \partial_y & 0 & \Delta^* \\ i\partial_x + \partial_y & -m_1 - m_4 & \Delta^* & 0 \\ 0 & \Delta & m_1 - m_4 & -i\partial_x - \partial_y \\ \Delta & 0 & -i\partial_x + \partial_y & -m_1 + m_4 \end{pmatrix} \\ &= -i\gamma_0\gamma_1\partial_x - i\gamma_0\gamma_2\partial_y + m_1 M_1 + \Delta M_2 + \Delta M_3 + m_4 M_4 \,. \end{aligned} \tag{2.48}$$

Since M_4 does not anticommute with M_1, M_2, and M_3, different behaviour is seen depending on the magnitudes of m_4 compared to m_{123}. Chamon *et al.* [7] examined how the charge is dependent on the ratio of $|m_4|/m_{123}$ for $m_{123} = 1$ with constant m_1. When $|m_4| = m_{123}$, the competition closes the gap. On the other hand, if $|m_4| < m_{123}$, the state has fractional charge with the same value as if there was no m_4. If $|m_4| > m_{123}$, $Q = 0$.

2.10 NN and NNN Interactions

The addition of nearest neighbour (NN) and next nearest neighbour (NNN) interactions to the tight-binding Hamiltonian H_0 in graphene can lead to a phase transition in graphene from a SM to one of the other insulating states (CDW, KBDW, QHE). Therefore, the following Hamiltonian is considered:

$$H = H_0 + H_{nn} + H_{nnn} \,, \tag{2.49}$$

where the NN interaction is:

$$H_{nn} = V_1 \sum_{\langle i,j \rangle} (n_i - 1)\,(n_j - 1) \,, \tag{2.50}$$

and the NNN interaction is:

$$H_{nnn} = V_2 \sum_{\langle\langle i,j \rangle\rangle} (n_i - 1)\,(n_j - 1) \,, \tag{2.51}$$

with (V_1, V_2) being the strength of the (NN, NNN) interaction, $(\langle i,j\rangle, \langle\langle i,j\rangle\rangle)$ are the (NN, NNN) links between sites $\vec{r}_i$ and $\vec{r}_j$, and $n_i = c_i^\dagger c_i$ is the number operator at $\vec{r}_i$.

The term $n_i n_j$ can be decomposed by mean-field theory into Hartree (on-site) and Fock (bond) channels. In the Hartree channel,

$$n_i n_j \approx n_i \langle n_j \rangle + \langle n_i \rangle n_j - \langle n_i \rangle \langle n_j \rangle \,, \tag{2.52}$$

where $\langle n_i \rangle$ is the mean occupation at $\vec{r}_i$, and the fluctuations $(n_i - \langle n_i \rangle)(n_j - \langle n_j \rangle)$ are neglected. Similarly, in the Fock channel,

$$n_i n_j = -\langle c_i^\dagger c_j \rangle \, c_j^\dagger c_i - \langle c_j^\dagger c_i \rangle \, c_i^\dagger c_j + \langle c_i^\dagger c_j \rangle \langle c_j^\dagger c_i \rangle \,. \tag{2.53}$$

The NN and NNN interaction in the Hartree channel modifies the Hamiltonian by:

$$H_p^{(h)} = 3\rho(V_1 - 2V_2) \sum_j n_j (-1)^j + 3N\rho^2 (V_1 - 2V_2)/2 \tag{2.54}$$

where $\rho = m_1$ is the order parameter for the CDW, and N is the total number of sites. The NN interaction in the Fock channel with a Kekulé pattern changes the hopping:

$$t'_a = t + V_1 \Delta_a \,, \tag{2.55}$$

with

$$\sum_{ij} V_1 \langle c_i^\dagger c_j \rangle \langle c_j^\dagger c_j \rangle = V_1 (\Delta_1^2 + \Delta_2^2 + \Delta_3^3) \, N/2 \,, \tag{2.56}$$

where $\Delta_a = \Delta \cos(\varphi + 2\pi/3)$ is the order parameter for the KBDW. If the hopping pattern is not staggered, the NN interaction in the Fock channel simply adds to the NN hopping term leaving graphene gapless. The NNN interaction in the Fock channel with directed hopping adds the following term to the Hamiltonian:

$$H_p^{(fnnn)} = V_2 \sum_{\langle\langle i,j \rangle\rangle} (\chi_{ij} c_i^\dagger c_j + h.c.) + 3NV_2(\chi_A^2 + \chi_B^2) \,, \tag{2.57}$$

where for next nearest neighbours i and j, $\langle c_i^\dagger c_j \rangle = \chi_{ij} = \pm i \chi_\alpha$ with α being site A or B and the sign chosen by the direction of hopping.

Weeks and Franz [56] found that the strength of the interactions leads to different phases. Small interactions strengths favour the SM. For $V_1/t \geq 0.93$ with $V_2/t = 0$, the CDW state is energetically preferred, while for $V_2/t \geq 1.20$ with $V_1/t = 0$, the QHE phase has the lowest energy. In between these two regions at higher interaction strengths, graphene is in the KBDW state.

2.11 Spinful Hamiltonian

The spinor can be enlarged from four components to eight by introducing spin up-down components. There are now 16 possible matrices that anticommute with the spinful Hamiltonian. The matrices are rewritten in terms of $X_{\mu\mu'\mu''} = \sigma_\mu \otimes \sigma_{\mu'} \otimes \sigma_{\mu''}$, where the first index is the Pauli matrix that represents spin. The Hamiltonian is a linear combination of X_{031} and X_{002}, and the four matrices representing the previously discussed insulating phases are X_{003} (CDW), X_{011} (Real KBDW) , X_{021} (Imaginary KBDW), and X_{033} (QHE). The new matrices that anticommute with the Hamiltonian are similar to the above four cases but with an added direction associated with the spin. $X_{103}, X_{203}, X_{303}$ are Néel ordering, or on-site spin density waves (SDW), in the x, y, z directions respectively. $X_{111}, X_{211}, X_{311}$ ($X_{121}, X_{221}, X_{321}$) are real (imaginary) KBDW in the x, y, z directions respectively. $X_{133}, X_{233}, X_{333}$ lead to Quantum Spin Hall effect (QSHE) in the x, y, z directions respectively where there are chiral edge currents which do not break time-reversal. In the QSHE state, although the Chern number is zero, there is a non-zero $\mathbb{Z}_2$ topological invariant ν which is the number of times the bands cross the Fermi energy mod 2. Kane and Mele [30] found that large spin-orbit coupling between next nearest neighbours can give rise to the QSHE. Unfortunately, this effect is not seen in graphene as the spin-orbit coupling is too small, but gapless edge states are seen in 2D HgTe/CdTe wells [31]. In 3D, there are topologically protected surface states and are seen in materials such as Bi_2Se_3 [59].

When including spin in the Hamiltonian, an on-site Hubbard interaction between the spins is added to the Hamiltonian $H = H_{0s} + H_U$:

$$H_{0s} = -\sum_{s=\uparrow,\downarrow} \sum_{r\in\Lambda_1} \sum_{i=1}^{3} \left[t\, c^\dagger_{r,s}\, c_{r+s_i,s} + h.c. \right] , \tag{2.58}$$

and

$$H_U = U \sum_{r\in\Lambda_1} \left(n_{r\uparrow}\, n_{r\downarrow} + n_{r+s_1\uparrow}\, n_{r+s_1\downarrow} \right) , \tag{2.59}$$

where $c^\dagger_{r,s}(c_{r,s})$ is the creation (annhilation) operator at $\vec{r}$, and $n_{rs} = c^\dagger_{r,s}\, c_{r,s}$ is the number operator at $\vec{r}$. The Hubbard term can be rewritten as follows:

$$H_U = \frac{U}{16} \sum_{r\in\Lambda_1} \sum_{s} (n_{rs} + n_{r+s_1 s})^2 + (n_{rs} - n_{r+s_1 s})^2 - \left[\sum_{s'} (\vec{f_r} + \vec{f}_{r+s_1})^2 + (\vec{f_r} - \vec{f}_{r+s_1})^2 \right] , \tag{2.60}$$

where $\vec{f}_r = c^\dagger_{r,s}\,\vec{\sigma}^{ss'}c_{r,s'}$. For the case with uniform average density, zero average magnetization, and finite Néel order, Herbut [22] found that it can be mapped to the case of non-zero CDW and KBDW order parameters in mean-field theory where the magnetization is $\vec{M} = \langle \vec{f}_r + \vec{f}_{r+s_1} \rangle$, and the Néel order parameter is $\vec{N} = \langle \vec{f}_r - \vec{f}_{r+s_1} \rangle$.

2.12 Superconductivity

Based on the work by Nambu [40], Bogoliubov [6], and Bardeen, Cooper, and Schrieffer [3], the Hamiltonian can be modified to take into account graphene in close proximity to a superconductor by enlarging the spinor to 16 components. In the Bogoliubov-deGennes (BdG) Hamiltonian, $H_{bdg} = \frac{1}{2}\int d^2r \Psi^\dagger H^{(bdg)} \Psi$ where

$$H_k^{(bdg)} = \begin{pmatrix} H_{pp} & H_{ph} \\ H_{ph}^\dagger & -H_{pp}^T \end{pmatrix}, \tag{2.61}$$

where $\Psi = (\psi_\uparrow, \psi_\downarrow, \psi_\uparrow^\dagger, \psi_\downarrow^\dagger)^T$ and $\psi_s = (\psi_{2-s}, \psi_{1-s}, \psi_{2+s}, \psi_{1+s})^T$ is the four component spinor with spin s. The fermionic annihilation operator, ψ_{abc}, acts on site a at Dirac point b with spin c. Writing out the possible matrices that anticommute with the Hamiltonian, there are 64 possibilities. Only 36 of those matrices satisfy the particle-hole constraint that a particle of energy E is linked to a hole of energy $-E$ [9]. The possible insulating states include those from the spinful Hamiltonian along with different classifications of singlet and triplet superconductivity [46].

2.13 Summary

Graphene can be changed from a semi-metal to an insulator by adding matrices that anticommute with the tight-binding Hamiltonian. These matrices correspond to a staggered chemical potential, Kekulé hopping, and directed NNN hopping. Furthermore, introducing topological defects such as domain walls, vortices, merons, and Skyrmions in the order parameters lead to bound-state solutions within the gap permitting fractional charge. To solve for the bound-state energies and their spinors, fourth-order differential equations are solved. The was done using a combination of polynomial expansion near $r = 0$ and finite difference methods. In particular, for a r-independent vortex with vorticity p, the bound-state energies

are numerically found at:

$$E_{p,l} = \mathrm{sgn}(l)\,\Delta_0\sqrt{1-[p/(|l|+|p|-1)]^2}\,, \tag{2.62}$$

with degeneracy $|l|+|p|-1$ where l is an odd integer. For a vortex which goes as r for $|p|=1$, the bound state energies are at $E_l = \mathrm{sgn}(l)\sqrt{2|l|}$ where l is an integer. For zero energy, $l=0$, the degeneracy is p which is the same as the r-independent case, but for $l \neq 0$, the degeneracy is $2|l|$.

In future work, analytical solutions for the r-independent vortex with vorticity p need to be explored. Also, the method presented can be used to solve more complicated configurations involving larger matrices due to the inclusion of spin and superconductivity. In some cases, the differential equations will decouple into known second or fourth-order differential equations.

Chapter 3

Phases on the Lieb Lattice

3.1 Lieb Lattice

Other lattices, such as the Lieb lattice as shown in Fig. 3.1, can also have a linear dispersion with phases different from graphene. The CuO_2 planes of high T_c cuprates such as $La_{1-x}Sr_xCuO_4$ and $YBa_2Cu_3O_7$ are Lieb lattices. They consist of a 2D square lattice with a 3-point basis (1,2,3). The primitive lattice vectors are $\vec{a}_1 = (2a, 0)$ and $\vec{a}_2 = (0, 2a)$ where a is half the lattice spacing. Sites 1 and 2 are connected by the $\vec{s}_{12} = (a, 0)$, and sites 1 and 3 are connected by $\vec{s}_{13} = (0, -a)$. Therefore, site 1 has 4 nearest neighbours whereas sites 2 and 3 only have 2 nearest neighbours. The Bravais lattice is therefore square, and the reciprocal primitive lattice vectors are $\vec{b}_1 = (\pi/a, 0)$, $\vec{b}_2 = (0, \pi/a)$. For convenience, the Brillouin zone is chosen to be the square defined by $\vec{b}_1$ and $\vec{b}_2$.

Using the tight-binding model for spinless fermions, the Hamiltonian without any interactions is:

$$H_0 = -t \left[\sum_{<1,2>} (c_1^\dagger c_2 + h.c.) + \sum_{<1,3>} (c_1^\dagger c_3 + h.c.) \right], \tag{3.1}$$

where $c_i^\dagger$ and c_i are the creation and annihilation operators at $\vec{r}_i$, $\langle i, j \rangle$ is the nearest neighbour (NN) link, and t is the NN hopping parameter.

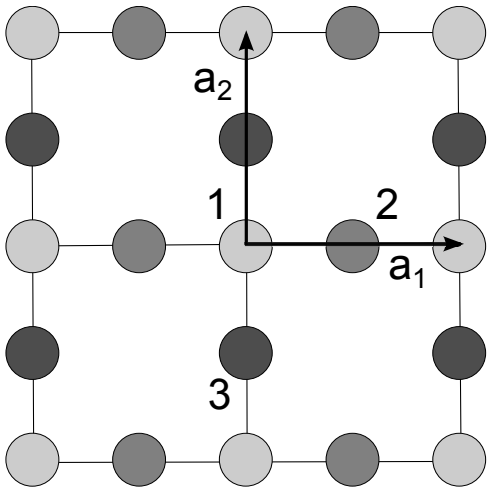

Figure 3.1: The Lieb lattice has three sites: light (1), medium (2), and dark (3). The primitive lattice vectors are $\vec{a}_1 = (2a, 0)$ and $\vec{a}_2 = (0, 2a)$ where a is half the lattice spacing.

Setting $a = 1$ and taking the Fourier transform, $H_0 = \sum_k \Psi_k^\dagger H_k^{(0)} \Psi_k$ where

$$\begin{aligned} H_k^{(0)} &= \begin{pmatrix} 0 & -2t\cos(k_x) & -2t\cos(k_y) \\ -2t\cos(k_x) & 0 & 0 \\ -2t\cos(k_y) & 0 & 0 \end{pmatrix} \\ &= -2t\left[\lambda_1 \cos(k_x) + \lambda_4 \cos(k_y)\right] , \end{aligned} \tag{3.2}$$

with $\Psi_k^\dagger = (c_{1k}^\dagger, c_{2k}^\dagger, c_{3k}^\dagger)$ and λ_j are the Gell-Mann matrices:

$$\lambda_1 = \begin{pmatrix} 0 & 1 & 0 \\ 1 & 0 & 0 \\ 0 & 0 & 0 \end{pmatrix}, \ \lambda_2 = \begin{pmatrix} 0 & -i & 0 \\ i & 0 & 0 \\ 0 & 0 & 0 \end{pmatrix},$$

$$\lambda_3 = \begin{pmatrix} 1 & 0 & 0 \\ 0 & -1 & 0 \\ 0 & 0 & 0 \end{pmatrix}, \ \lambda_4 = \begin{pmatrix} 0 & 0 & 1 \\ 0 & 0 & 0 \\ 1 & 0 & 0 \end{pmatrix},$$

$$\lambda_5 = \begin{pmatrix} 0 & 0 & -i \\ 0 & 0 & 0 \\ i & 0 & 0 \end{pmatrix}, \ \lambda_6 = \begin{pmatrix} 0 & 0 & 0 \\ 0 & 0 & 1 \\ 0 & 1 & 0 \end{pmatrix},$$

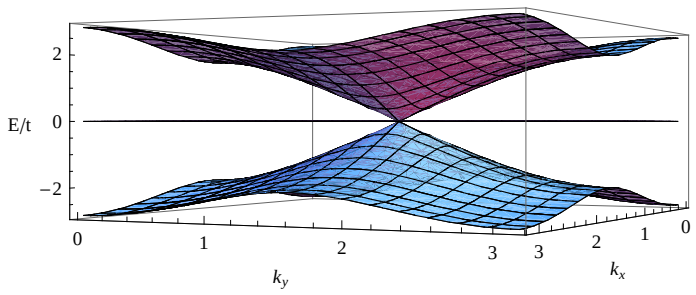

Figure 3.2: The energy dispersion for the tight-binding Lieb lattice without interactions consists of a single Dirac cone with a flat band.

$$\lambda_7 = \begin{pmatrix} 0 & 0 & 0 \\ 0 & 0 & -i \\ 0 & i & 0 \end{pmatrix}, \; \lambda_8 = \frac{1}{\sqrt{3}} \begin{pmatrix} 1 & 0 & 0 \\ 0 & 1 & 0 \\ 0 & 0 & -2 \end{pmatrix}, \tag{3.3}$$

such that $[g_i, g_j] = i f_{ijk} g_k$ with $g_j = \lambda_j/2$, $f_{123} = 1$, $f_{147} = f_{165} = f_{246} = f_{257} = f_{345} = f_{376} = 1/2$, and $f_{458} = f_{678} = \sqrt{3}/2$.

The energy dispersion has a Dirac cone and a flat band.

$$E_k = \begin{pmatrix} \pm 2t\sqrt{\cos^2(k_x) + \cos^2(k_y)} \\ 0 \end{pmatrix}. \tag{3.4}$$

For the Brillouin zone defined by $0 \leq k_x \leq \pi$ and $0 \leq k_y \leq \pi$, all three bands touch at $k_x = k_y = \pi/2$ as shown in Fig. 3.2. If the Brillouin zone is chosen such that $-\pi/2 \leq k_x \leq \pi/2$ and $-\pi/2 \leq k_y \leq \pi/2$, all three bands touch at the four corner points. Only one is inequivalent since all the points are related by reciprocal lattice vectors. Near $k_x = k_y = \pi/2$, $E_p = \{\pm 2t|\vec{p}|, 0\}$ where $p_j = (k_j - \pi/2)$. For one-third filling at T = 0, only the lowest band is filled, and the system is a semi-metal (SM). Defining the number operator $n_i = c_i^\dagger c_i$ and diagonalizing the matrix, the occupation at sites $(1, 2, 3)$ are $(\frac{1}{2}, \frac{1}{4}, \frac{1}{4})$.

3.2 Nearest Neighbour (NN) Interaction

The NN interaction term on the Lieb lattice is:

$$H_{nn} = V_1 \left[\sum_{<1,2>} \left(n_1 - \frac{1}{2}\right)\left(n_2 - \frac{1}{4}\right) + \sum_{<1,3>} \left(n_1 - \frac{1}{2}\right)\left(n_3 - \frac{1}{4}\right) \right]. \tag{3.5}$$

In the Hartree channel, there are two possible order parameters to define the occupation on the three sites: charge density wave (CDW) and broken $\pi/2$ rotation symmetry (BR). The CDW order parameter, $\delta = (n_1 - n_2 - n_3)/4$, is proportional to the difference in occupation between site 1 and the sum of sites 2 and 3. The BR order parameter, $\eta = (n_2 - n_3)/2$, is proportional to the difference in occupation between sites 2 and 3. Therefore, at one-third filling, $n_1 = 1/2 + 2\delta$, $n_2 = 1/4 - \delta + \eta$, and $n_3 = 1/4 - \delta - \eta$ where $\delta = \eta = 0$ for the SM. Since the filling does not change with the interaction, there is a one-third filling constraint: $n_1 + n_2 + n_3 = 1$. As a result, $H_{hnn} = \sum_k \Psi_k^\dagger H_k^{(hnn)} \Psi_k + 8N_1V_1\delta^2$ where

$$H_k^{(hnn)} = \begin{pmatrix} -4V_1\delta & 0 & 0 \\ 0 & 4V_1\delta & 0 \\ 0 & 0 & 4V_1\delta \end{pmatrix}, \tag{3.6}$$

and N_1 is the number of site 1.

The NN interaction in the Hartree channel does not break the rotation symmetry and anticommutes with H_0. Therefore, the tight-binding Hamiltonian with the Hartree NN interaction $(H_0 + H_{hnn})$ is gapped and has the following dispersion:

$$E_k = \begin{pmatrix} \pm 2\sqrt{4V_1^2\delta^2 + t^2\cos^2(k_x) + t^2\cos^2(k_y)} \\ 4V_1\delta \end{pmatrix}. \tag{3.7}$$

For $\delta > 0$, the flat band touches the upper band, while for $\delta < 0$, the flat band touches the lower band as shown in Fig. 3.3. For one-third filling, the free energy is:

$$F = \sum_k -2\sqrt{4V_1^2\delta^2 + t^2\cos^2(k_x) + t^2\cos^2(k_y)} + 8N_1V_1\delta^2\,, \tag{3.8}$$

Minimizing the free energy with respect to δ gives a self-consistent equation for δ given V_1:

$$\frac{dF}{d\delta} = 0 = \sum_k \frac{-8V_1^2\delta}{\sqrt{4V_1^2\delta^2 + t^2\cos^2(k_x) + t^2\cos^2(k_y)}} + 16N_1V_1\delta\,. \tag{3.9}$$

As the interaction strength increases, comparing the free energy of the SM and CDW states shows that CDW is favoured for $V_1 > V_{1c}^{(hnn)}/t = 1.555$. For V_1 near and just larger than $V_{1c}^{(hnn)}$, δ changes linearly with $(V_1 - V_{1c}^{(hnn)})/t$. As V_1 increases, δ approaches $\pm\frac{1}{4}$. For $\delta = \frac{1}{4}$, $(n_1, n_2, n_3) = (1, 0, 0)$, and for $\delta = -\frac{1}{4}$, $(n_1, n_2, n_3) = (0, \frac{1}{2}, \frac{1}{2})$. Because the Hartree interaction is classical, the occupation can only be non-negative integers, and therefore, a gap opens since δ must approach $\frac{1}{4}$ as shown in Fig. 3.5. Occupation of one of the three sites in this limit is expected since the interaction is repulsive.

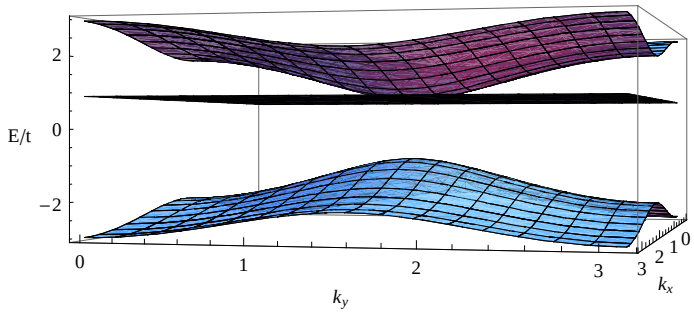

Figure 3.3: Energy dispersion for the tight-binding Lieb lattice with only the NN interaction in the Hartree channel($V_1/t = 2$, $\delta = 0.1129$).

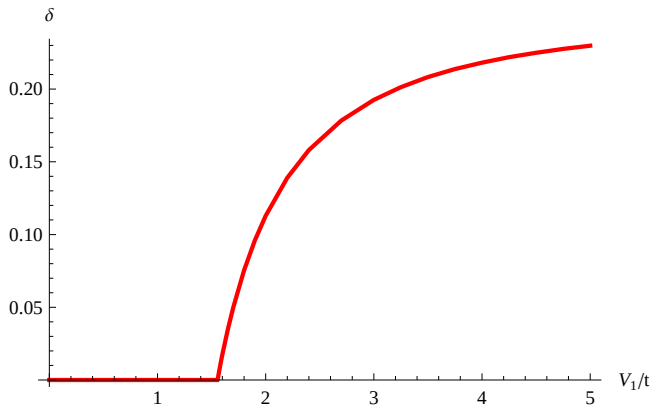

Figure 3.4: In the tight-binding Lieb lattice with only the NN interaction in the Hartree channel, near the transition from SM-CDW, $\delta = 0.392(V_1 - V_{1c}^{(hnn)})/t$. As $V_1/t \to \infty$, δ approaches $\frac{1}{4}$.

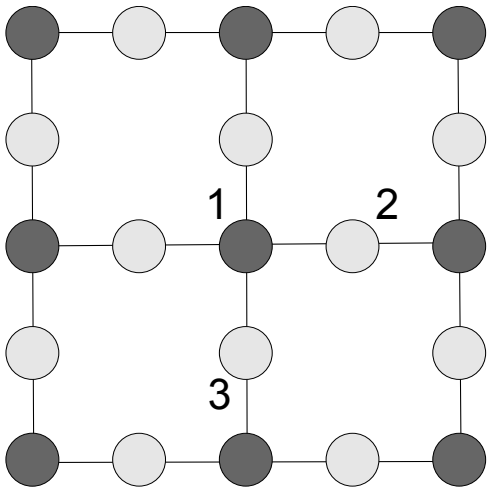

Figure 3.5: For the tight-binding Lieb lattice with only the NN interaction in the Hartree channel, as V_1 increases, occupation on site 1 is favoured (dark) over sites 2 and 3 (light); $\delta \to \frac{1}{4}$.

In the Fock channel, if the hopping is dimerized (NN hopping from sites 1 larger in positive direction than negative direction) as shown in Fig. 3.6, a gap is also opened. Defining the dimer order parameter $\epsilon = \langle c_1^\dagger c_j \rangle (r_{jx} + r_{jy} - r_{1x} - r_{1y}) = \langle c_j^\dagger c_1 \rangle (r_{jx} + r_{jy} - r_{1x} - r_{1y})$ where (r_{jx}, r_{jy}) is the position of site j, and sites 1 and j are NN, the resulting NN interaction in the Fock channel with staggered hopping is $H_{fnn} = \sum_k \Psi_k^\dagger H_k^{(fnn)} \Psi_k + 4N_1 V_1 \epsilon^2$ with

$$H_k^{(fnn)} = \begin{pmatrix} 0 & -2iV_1\epsilon\sin(k_x) & -2iV_1\epsilon\sin(k_y) \\ 2iV_1\epsilon\sin(k_x) & 0 & 0 \\ 2iV_1\epsilon\sin(k_y) & 0 & 0 \end{pmatrix}. \tag{3.10}$$

The energy dispersion for the tight-binding model with NN interaction in the Fock channel with staggered hopping $(H_0 + H_{fnn})$ is:

$$E_k = \begin{pmatrix} \pm 2\sqrt{V_1^2\epsilon^2[\sin^2(k_x) + \sin^2(k_y)] + t^2\cos^2(k_x) + t^2\cos^2(k_y)} \\ 0 \end{pmatrix}. \tag{3.11}$$

For $\epsilon \neq 0$, the spectrum is symmetrically gapped. Minimizing the free energy with respect to ϵ reveals the transition from SM to a dimer state for $V_{1c}^{(fnn)}/t > 2.479$. Near the transition, the dimer order parameter varies linearly with $(V_1 - V_{1c}^{(fnn)})/t$. As the interaction strength

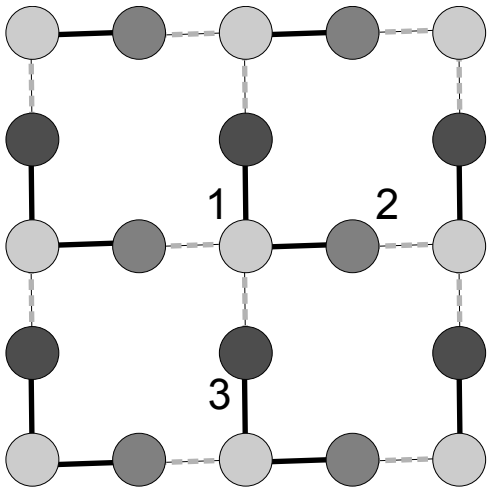

Figure 3.6: The tight-binding Lieb lattice with only NN interaction in the Fock channel with staggered hopping. NN hopping from sites 1 is larger in the positive direction (solid dark lines) than in the negative direction (dashed light lines).

increases, the order parameter can be solved analytically. It is found to analytically approach ≈ 0.2395 as shown in Fig. 3.8. If the Fock channel is not staggered, the interaction would simply add to the hopping parameter (and therefore not create a gap).

When NN interactions with both Hartree and Fock channels with staggered hopping in the tight-binding model, $H_0 + H_{hnn} + H_{fnn}$, are considered, the resulting dispersion relation is:

$$E_k = \begin{pmatrix} \pm 2\sqrt{V_1^2[4\delta^2 + \epsilon^2\sin^2(k_x) + \epsilon^2\sin^2(k_y)] + t^2[\cos^2(k_x) + \cos^2(k_y)]} \\ 4V_1\delta \end{pmatrix} . \tag{3.12}$$

There are two self-consistent equations that arise from minimizing the free energy with respect to δ and by minimizing the free energy with respect to ϵ:

$$\sum_k \frac{V_1\delta}{\sqrt{V_1^2[4\delta^2 + \epsilon^2\sin^2(k_x) + \epsilon^2\sin^2(k_y)] + t^2[\cos^2(k_x) + \cos^2(k_y)]}} = 2N_1\delta\,. \tag{3.13}$$

$$\sum_k \frac{V_1\epsilon[\sin^2(k_x) + \sin^2(k_y)]}{\sqrt{V_1^2[4\delta^2 + \epsilon^2\sin^2(k_x) + \epsilon^2\sin^2(k_y)] + t^2[\cos^2(k_x) + \cos^2(k_y)]}} = 4N_1\epsilon\,. \tag{3.14}$$

The solution to these equations is the same as if there is no Fock channel. For $V_1 < V_{1c}^{(hnn)}$, $\delta = \epsilon = 0$, while for $V_1 > V_{1c}^{(hnn)}$, $\delta \neq 0$ and $\epsilon = 0$.

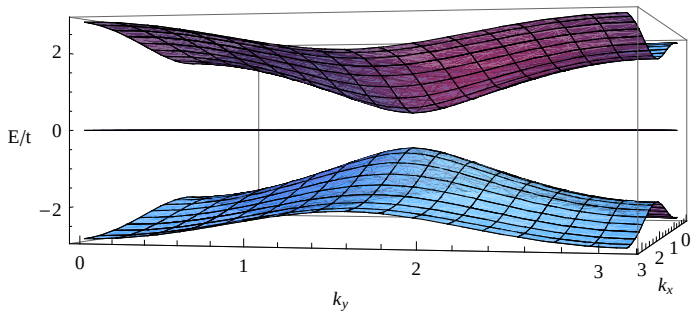

Figure 3.7: Energy dispersion for the tight-binding Lieb lattice with only the NN interaction in the Fock channel with staggered hopping ($V_1/t = 3$, $\epsilon = 0.0611$).

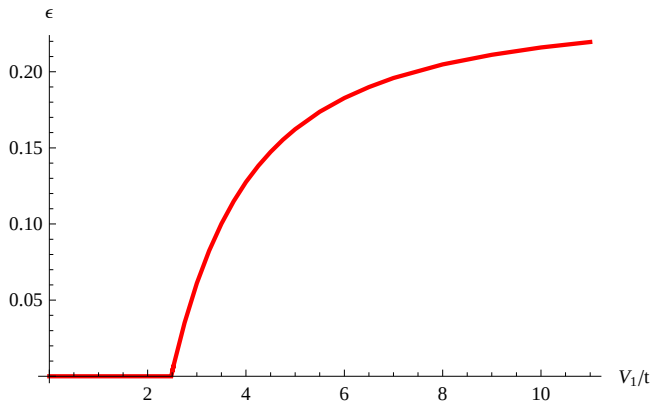

Figure 3.8: In the tight-binding Lieb lattice with only the NN interaction in the Fock channel with staggered hopping, near the transition from SM-dimer, $\epsilon = 0.140(V_1 - V_{1c}^{(fnn)})/t$. As $V_1 \to \infty$, ϵ analytically approaches ≈ 0.2395.

3.3 Next Nearest Neighbour (NNN) Interaction

The NNN interaction in mean-field theory adds the following term to the Hamiltonian:

$$H_{nnn} = V_2 \left[\sum_{<2,3>} \left(n_2 - \frac{1}{4} \right) \left(n_3 - \frac{1}{4} \right) \right] . \tag{3.15}$$

For the NNN interaction in the Fock channel, a gap is created when time reversal symmetry is broken (BTR). This state breaks the time reversal symmetry through directed NNN hopping as illustrated in Fig. 3.9. The BTR order parameter χ is defined such that $\langle c_a^\dagger c_b \rangle = i\chi(a-b)[2(r_{ax}-r_{bx})(r_{ay}-r_{by})-1]$ where (r_{ax}, r_{ay}) is the position of site a, χ is a nonnegative real number and a and b are next nearest neighbours. The NNN interaction in the Fock channel with directed hopping is $H_{fnnn} = \sum_k \Psi_k^\dagger H_k^{(fnnn)} \Psi_k + 4N_2V_2\chi^2$ where

$$H_k^{(fnnn)} = \begin{pmatrix} 0 & 0 & 0 \\ 0 & 0 & 4iV_2\chi \sin(k_x)\sin(k_y) \\ 0 & -4iV_2\chi \sin(k_x)\sin(k_y) & 0 \end{pmatrix} . \tag{3.16}$$

Unlike the NN interaction, the NNN interaction in the Hartree and Fock channels must be considered together because the CDW order parameter changes with the BTR order parameter. The NNN interaction in the Hartree and Fock channels is $H_{hfnnn} = \sum_k \Psi_k^\dagger H_k^{(hfnnn)} \Psi_k + N_2V_2(4\eta^2 - 4\delta^2 + 2\delta + 4\chi^2)$ where

$$H_k^{(hfnnn)} = \begin{pmatrix} 0 & 0 & 0 \\ 0 & -4V_2\delta - 4V_2\eta & 4iV_2\chi \sin(k_x)\sin(k_y) \\ 0 & -4iV_2\chi \sin(k_x)\sin(k_y) & -4V_2\delta + 4V_2\eta \end{pmatrix} . \tag{3.17}$$

Solving the three self-consistent equations from minimizing the free energy from $H_0 + H_{hfnnn}$ at one-third filling, there is a transition from SM to a BR phase at $V_{2c}/t = 1.133$. The BR phase has $\eta \neq 0$, $\delta \neq 0$, and $\chi = 0$. Near the critical point, the order parameters do not vary linearly with $(V_2 - V_{2c})/t$ as more than one order parameter changes simultaneously. As V_2 becomes large, δ and η approach $-\frac{1}{4}$ and $\pm\frac{1}{2}$ respectively. Therefore, the occupation of the sites $(1, 2, 3)$ is either $(0, 1, 0)$ or $(0, 0, 1)$. An example of the energy dispersion of the BR phase is shown in Fig. 3.10. There exists a BTR solution that satisfies the three self-consistent equations with $\chi \neq 0$, $\delta \neq 0$, and $\eta = 0$. The free energy for this phase is always higher than the BR, but lower than the SM for $V_2/t > 1.859$. As a result, the solution to the tight-binding model with the NNN interaction in the Hartree and Fock channels with

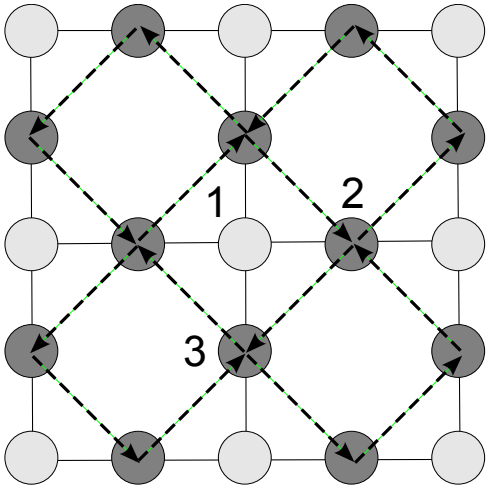

Figure 3.9: Directed NNN links as shown above lead to the BTR state in the Lieb lattice.

directed NNN hopping is the same as with only the NNN interaction in the Hartree channel since the BTR phase is never favoured.

3.4 NN and NNN Interactions

Combining both NN and NNN interactions in the spinless tight-binding Lieb Lattice ($H_0 + H_{hnn} + H_{fnn} + H_{hfnnn}$) opens up the possibility of six different phases: SM, dimer, CDW, BR, BTR, or a combination of the states. Since the latter three all change the CDW order parameter, it is not intuitive how the phase diagram will look. From solving for the lowest band, constructing the free energy, and minimizing the free energy for the lowest energy states, the resulting phase diagram is shown in Fig. 3.12. As expected, when $V_2/t = 0$, the CDW state is favoured for $V_1 > V_{1c}^{(hnn)}$, and when $V_1/t = 0$, the BR state has the lowest energy after V_{2c}/t. Going from SM to CDW is a second order transition, and the critical values of V_1/t and V_2/t follow $V_1/t = 1.555 + 0.5V_2/t$. There are regions where the BTR phase is favoured ($\chi \neq 0$, $\delta \neq 0$, and $\eta = 0$) and χ is quite small, being between 0 and 0.0140. In addition, there is a large region where the BR phase is preferred ($\eta \neq 0$, $\delta \neq 0$, and $\chi = 0$). Between these regions is a combined BTR and BR phase ($\eta \neq 0$, $\delta \neq 0$, and $\chi \neq 0$). The transitions between these three phases are second order. In the CDW phase, $\delta > 0$, while $\delta < 0$ in the current phase, and therefore, the transition from CDW to the

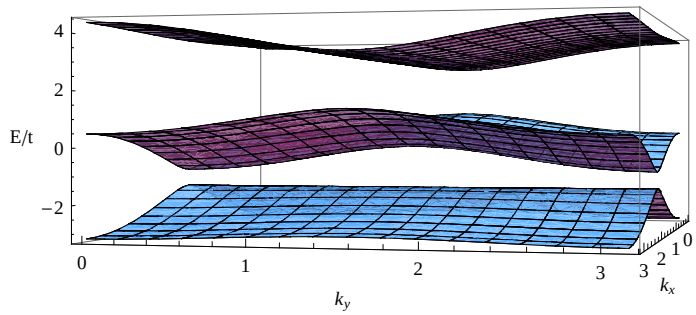

Figure 3.10: Energy dispersion for the tight-binding Lieb lattice with only Hartree NNN interaction ($V_1/t = 1.7$, $\delta = 0.1262$, $\eta = 0.3612$). In the tight-binding Lieb lattice with only Hartree NNN interaction, the phase changes from SM to BR at $V_2/t = 1.133$ as δ and η become nonzero.

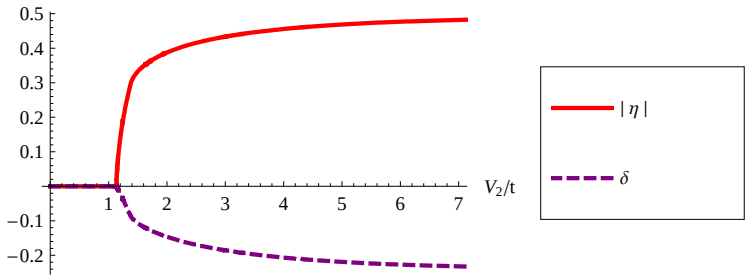

Figure 3.11: For strong V_2/t, there are two degenerate solutions: occupation only on site 2 ($\delta = -\frac{1}{4}$, $\eta = \frac{1}{2}$) or only on site 3 ($\delta = -\frac{1}{4}$, $\eta = -\frac{1}{2}$).

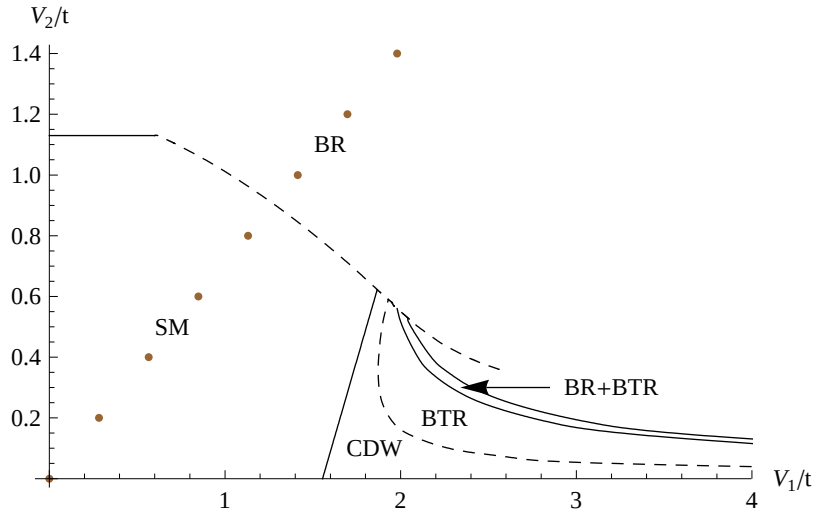

Figure 3.12: Phase diagram for the Lieb lattice. Solid lines indicate second order phase transitions, while dashed lines indicate first order phase transitions. The dots represent the line along which the ratio V_2/V_1 would be expected to fall based on a crude estimate of the bare Coloumb repulsion.

BTR state is first order. When the phase changes from SM to BR, the transition can be first or second order depending on V_1/t. For $V_1/t < 0.6$, the transition is second order as both δ and η change continuously. On the other hand, $V_1/t > 0.6$, the transition is first order as both δ and η are discontinuous across the transition. Within the BR phase, there is a discontinuity in the δ and η order parameters as shown in Fig. 3.12. Notice that there is no dimer state in the phase diagram.

3.5 Summary

Spinless fermions on the Lieb lattice exhibit different behaviour than on a hexagonal lattice, like graphene. On the Lieb lattice, there are three sites per unit cell resulting in three bands: a Dirac cone with a flat band. The different phases that occur due to nearest and next nearest neighbour interactions where only the lowest band is filled was solved in mean-field theory. When only the nearest neighbour interaction is considered, there is a transition from a semi-metallic phase to a charge density wave where site 1 is favoured over sites 2 and 3. On the other hand, when examining only the next nearest neighbour interaction, the

(a)

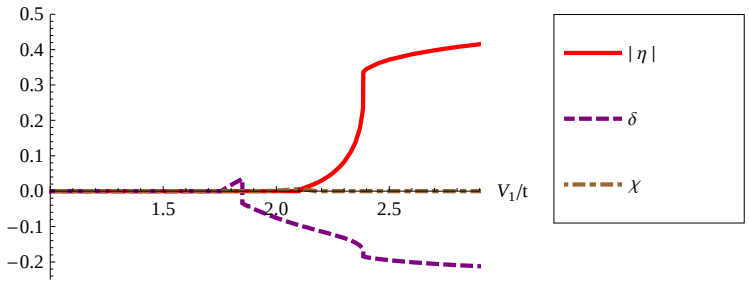

(b)

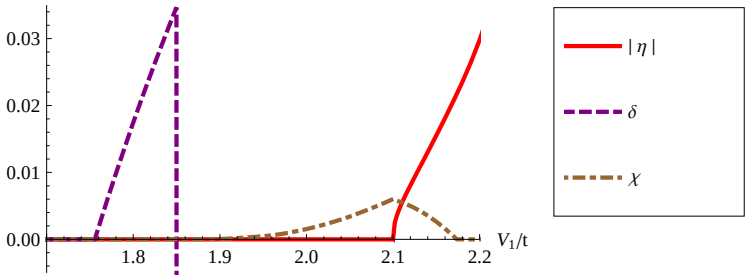

Figure 3.13: How the order parameters change as a function of V_1/t with $V_2/t = 0.4$. (a) The phase changes from SM-CDW at $V_2/t = 1.756$ to BTR at $V_2/t = 1.875$ to (BTR+BR) at $V_2/t = 2.098$ to BR at $V_2/t = 2.174$ to another BR discontinuously at $V_2/t = 2.385$. The CDW order parameter δ changes discontinuously from positive to negative at $V_2/t = 1.875$ since the CDW favours $\delta > 0$, while BTR wants $\delta < 0$. (b) The region $1.7 < V_1/t < 2.2$ is enlarged clearly showing the nonzero values of χ and η.

phase changes from a semi-metal to a broken $\pi/2$ rotation state where site 2 or 3 is preferred over site 1. When both interactions are added to the Hamiltonian, there are regions where broken time reversal is energetically favourable.

In future work, the phase diagram for spinless fermions on the Lieb lattice at two-thirds filling can be examined in mean-field theory. Also, the Hamiltonian can be expanded to include spin by introducing the Hubbard term. The new phase diagram will possibly have spin density waves (SDW), spin dimers, spin broken $\pi/2$ rotation, directed next nearest neighbour hopping without breaking time reversal, or combinations of these states. Lastly, to calculate the higher order corrections to the mean-field results, fluctuations can be taken into account by using random phase approximation or renormalization group theory.

Bibliography

[1] T. Ando. Theory of Electronic States and Transport in Carbon Nanotubes. *Journal of the Physical Society of Japan*, 74:777–817, 2005.

[2] T. Ando, Y. Matsumoto, and Y. Uemura. Theory of Hall Effect in a Two-Dimensional Electron System. *Journal of the Physical Society of Japan*, 39:279–288, 1975.

[3] J. Bardeen, L. N. Cooper, and J. R. Schrieffer. Theory of Superconductivity. *Physical Review*, 108:1175–1204, 1957.

[4] C. W. J. Beenakker. Specular Andreev Reflection in Graphene. *Physical Review Letters*, 97:067007–1–4, 2006.

[5] C. Berger, Z. Song, T. Li, X. Li, A. Y. Ogbazghi, R. Feng, Z. Dai, A. N. Marchenkov, E. H. Conrad, P. N. First, and W. A. de Heer. Ultrathin Epitaxial Graphite: 2D Electron Gas Properties and a Route toward Graphene-based Nanoelectronics. *Journal of Physical Chemistry B*, 108:19912–19916, 2004.

[6] N. N. Bogoliubov. On a New Method in the Theory of Superconductivity. *Journal of Experimental and Theoretical Physics*, 34:58–65, 1958.

[7] C. Chamon, C.-Y. Hou, R. Jackiw, C. Mudry, S.-Y. Pi, and A. P. Schnyder. Irrational Versus Rational Charge and Statistics in Two-Dimensional Quantum Systems. *Physical Review Letters*, 100:110405–1–4, 2008.

[8] C. Chamon, C.-Y. Hou, R. Jackiw, C. Mudry, S.-Y. Pi, and G. Semenoff. Electron fractionalization for two-dimensional Dirac fermions. *Physical Review B*, 77:235431–1–13, 2008.

[9] C. Chamon, C.-Y. Hou, C. Mudry, S. Ryu, and L. Santos. Masses and Majorana fermions in graphene. *Physica Scripta*, 2012:014013–1–7, 2012.

[10] Z. Chen, W. Ren, L. Gao, B. Liu, S. Pei, and H.-M. Cheng. Three-dimensional flexible and conductive interconnected graphene networks grown by chemical vapour deposition. *Nature Materials*, 10:424–428, 2011.

[11] J. Coraux, A. T. N'Diaye, C. Busse, and T. Michely. Structural Coherency of Graphene on Ir(111). *Nano Letters*, 8:565–570, 2008.

[12] M. S. Dresselhaus and G. Dresselhaus. Intercalation compounds of graphite. *Advances in Physics*, 51:1–186, 2002.

[13] K. V. Emtsev, A. Bostwick, K. Horn, J. Jobst, G. L. Kellogg, L. Ley, J. L. McChesney, T. Ohta, S. A. Reshanov, J. Röhrl, E. Rotenberg, A. K. Schmid, D. Waldmann, H. B. Weber, and T. Seyller. Towards wafer-size graphene layers by atmospheric pressure graphitization of silicon carbide. *Nature Materials*, 8:203–207, 2009.

[14] P. Ghaemi, S. Ryu, and D.-H. Lee. Quantum valley Hall effect in proximity-induced superconducting graphene: An experimental window for deconfined quantum criticality. *Physical Review B*, 81:081403–1–4, 2010.

[15] N. Goldman, D. F. Urban, and D. Bercioux. Topological phases for fermionic cold atoms on the Lieb lattice. *Physical Review A*, 83:063601–1–11, 2011.

[16] D. F. Greenberger. Accidental Degeneracy. *American Journal of Physics*, 34:1101–1109, 1966.

[17] T. Grover and T. Senthil. Topological Spin Hall States, Charged Skyrmions, and Superconductivity in Two Dimensions. *Physical Review Letters*, 100:156804–1–4, 2008.

[18] F. Guinea, B. Horovitz, and P. Le Doussal. Gauge field induced by ripples in graphene. *Physical Review B*, 77:205421–1–8, 2008.

[19] F. D. M. Haldane. Model for a Quantum Hall Effect without Landau Levels: Condensed-Matter Realization of the Parity Anomaly. *Physical Review Letters*, 61:2015–2018, 1988.

[20] E. H. Hall. On a New Action of the Magnet on Electric Currents. *American Journal of Mathematics*, 2:287–292, 1879.

[21] M. Z. Hasan and C. L. Kane. Topological Insulators. *Reviews of Modern Physics*, 82:3045–3067, 2010.

[22] I. F. Herbut. Zero-Energy States and Fragmentation of Spin in the Easy-Plane Antiferromagnet on a Honeycomb Lattice. *Physical Review Letters*, 99:206404–1–4, 2007.

[23] I. F. Herbut and C.-K. Lu. Antilinear spectral symmetry and the vortex zero-modes in topological insulators and graphene. *Physical Review B*, 82:125402–1–5, 2010.

[24] I. F. Herbut and C.-K. Lu. Spectrum of the Dirac Hamiltonian with the mass-hedgehog in arbitrary dimension. *Physical Review B*, 83:125412–1–6, 2010.

[25] C.-Y. Hou, C. Chamon, and C. Mudry. Electron Fractionalization in Two-Dimensional Graphenelike Structures. *Physical Review Letters*, 98:186809–1–4, 2007.

[26] R. Jackiw and S.-Y. Pi. Chiral Gauge Theory for Graphene. *Physical Review Letters*, 98:266402–1–4, 2007.

[27] R. Jackiw and C. Rebbi. Solitons with fermion number 1/2. *Physical Review D*, 13:3398–3409, 1976.

[28] R. Jackiw and P. Rossi. Zero modes of the vortex-fermion system. *Nuclear Physics B*, 190:681–691, 1981.

[29] J. M. Jauch and E. L. Hill. On the Problem of Degeneracy in Quantum Mechanics. *Physical Review*, 57:641–645, 1940.

[30] C. L. Kane and E. J. Mele. Quantum Spin Hall Effect in Graphene. *Physical Review Letters*, 95:226801–1–4, 2005.

[31] M. König, S. Wiedmann, C. Brüne, A. Roth, H. Buhmann, L. W. Molenkamp, X.-L. Qi, and S.-C. Zhang. Quantum Spin Hall Effect in Graphene. *Science*, 318:766–770, 2007.

[32] J. Kwak, J. H. Chu, J.-K. Choi, S.-D. Park, H. Go, S. Y. Kim, K. Park, S.-D. Kim, Y.-W. Kim, E. Yoon, S. Kodambaka, and S.-Y. Kwon. Near room-temperature synthesis of transfer-free graphene films. *Nature Communications*, 3:645–1–7, 2012.

[33] R. B. Laughlin. The Anomalous Quantum Hall Effect: An Incompressible Quantum Fluid with Fractionally Charged Excitations. *Physical Review Letters*, 50:1395–1398, 1983.

[34] C. Lee, X. Wei, J. W. Kysar, and J. Hone. Measurement of the elastic properties and intrinsic strength of monolayer graphene. *Science*, 321:385–388, 2008.

[35] S.-K. Lee, B. J. Kim, H. Jang, S. C. Yoon, C. Lee, B. H. Hong, J. A. Rogers, J. H. Cho, and J.-H. Ahn. Stretchable graphene transistors with printed dielectrics and gate electrodes. *Nano Letters*, 11:4642–4646, 2011.

[36] X. S. Li, W. W. Cai, J. H. An, S. Kim, J. Nah, D. X. Yang, R. Piner, A. Velamakanni, I. Jung, E. Tutuc, S. K. Banerjee, L. Colombo, and R. S. Ruoff. Large-Area Synthesis of High-Quality and Uniform Graphene Films on Copper Foils. *Science*, 324:1312–1314, 2009.

[37] C.-K. Lu and I. F. Herbut. Supersymmetric Runge-Lenz-Pauli vector for Dirac vortex in topological insulators and graphene. *Journal of Physics A: Mathematical and Theoretical*, 44:295003–1–13, 2011.

[38] C.-K. Lu and I. F. Herbut. Zero modes and charged Skyrmions in graphene bilayer. electronic preprint: arXiv: 12026047v1.

[39] R. R. Nair, P. Blake, A. N. Grigorenko, K. S. Novoselov, T. J. Booth, T. Stauber, N. M. R. Peres, and A. K. Geim. Fine Structure Constant Defines Visual Transparency of Graphene. *Science*, 320:1308, 2008.

[40] Y Nambu. Quasi-Particles and Gauge Invariance in the Theory of Superconductivity. *Physical Review*, 117:648–663, 1960.

[41] K. S. Novoselov, A. K. Geim, S. V. Marozov, D. Jiang, Y. Zhang, S. V. Dubonos, I. V. Grigorieva, and A. A. Firsov. Electric Field Effect in Atomically Thin Carbon Films. *Science*, 306:666–669, 2004.

[42] A. N. Obraztsov, E. A. Obraztsova, A. V. Tyurnina, and A. A. Zolotukhin. Chemical vapor deposition of thin graphite films of nanometer thickness. *Carbon*, 45:2017–2021, 2007.

[43] S. Raghu, X.-L. Qi, C. Honerkamp, and S.-C. Zhang. Topological Mott Insulators. *Physical Review Letters*, 100:156401–1–5, 2008.

[44] D. L. Rode. Electron Transport in InSb, InAs, and InP. *Physical Review B*, 3:3287–3299, 1971.

[45] B. Roy and I. F. Herbut. Unconventional superconductivity on honeycomb lattice: the theory of Kekulé order parameter. *Physical Review B*, 82:035429–1–7, 2010.

[46] S. Ryu, C. Mudry, C.-Y. Hou, and C. Chamon. Masses in graphenelike two-dimensional electronic systems: Topological defects in order parameters and their fractional exchange statistics. *Physical Review B*, 80:205319–1–32, 2009.

[47] R. Saito, M. S. Dresselhaus, and G. Dresselhaus. *Physical Properties of Carbon Nanotubes*. Imperial College Press: London, 1998.

[48] F. Schedin, A. K. Geim, S. V. Morozov, E. W. Hill, P. Blake, M. I. Katsnelson, and K. S. Novoselov. Detection of individual gas molecules adsorbed on graphene. *Nature Materials*, 6:652–655, 2007.

[49] G. W. Semenoff. Condensed-Matter Simulation of a Three-Dimensional Anomaly. *Physical Review Letters*, 53:2449–2452, 1984.

[50] B. Seradjeh. Midgap spectrum of the fermion-vortex system. *Nuclear Physics B*, 805:182–189, 2008.

[51] W. P. Su, J. R. Schrieffer, and A. J. Heeger. Solitons in Polyacetylene. *Physical Review Letters*, 42:1698–1701, 1979.

[52] L. M. Viculis, J. J. Mack, and R. B. Kaner. A Chemical Route to Carbon Nanoscrolls. *Science*, 299:1361, 2003.

[53] K. von Klitzing, G. Dorda, and M. Pepper. New Method for High-Accuracy Determination of the Fine-Structure Constant Based on Quantized Hall. *Physical Review Letters*, 45:494–497, 1980.

[54] P. R. Wallace. The Band Theory of Graphite. *Physical Review*, 71:622–634, 1947.

[55] X. Wang, L. Zhi, and K. Müllen. Transparent, Conductive Graphene Electrodes for Dye-Sensitized Solar Cells. *Nano Letters*, 8:323–327, 2008.

[56] C. Weeks and M. Franz. Interaction driven instabilities of a Dirac semi-metal. *Physical Review B*, 81:085105–1–8, 2010.

[57] J. Wu, M. Agrawal, H. A. Becerril, Z. Bao, Z. Liu, Y. Chen, and P. Peumans. Organic Light-Emitting Diodes on Solution-Processed Graphene Transparent Electrodes. *ACS Nano*, 4:43–48, 2010.

[58] Y. Wu, Y.-M. Lin, A. A. Bol, K. A. Jenkins, F. Xia, D. B. Farmer, Y. Zhu, and P. Avouris. High-frequency, scaled graphene transistors on diamond-like carbon. *Nature*, 472:74–78, 2011.

[59] Y. Xia, D. Qian, D. Hsieh, L. Wray, A. Pal, H. Lin, A. Bansil, D. Grauer, Y. S. Hor, R. J. Cava, and M. Z. Hasan. Observation of a large-gap topological-insulator class with a single Dirac cone on the surface. *Nature Physics*, 5:398–402, 2009.

[60] F. Yavari, Z. Chen, A. V. Thomas, W. Ren, H.-M. Cheng, and N. Koratkar. High sensitivity gas detection using a macroscopic three-dimensional graphene foam network. *Scientific Reports*, 1:166–1–5, 2009.

[61] H. Zhang, C.-X. Liu, X.-L. Qi, X. Dai, Z. Fang, and S.-C. Zhang. Topological insulators in Bi_2Se_3, Bi_2Te_3 and Sb_2Te_3 with a single Dirac cone on the surface. *Nature Physics*, 5:438–442, 2009.

[62] Y. Zheng and T. Ando. Hall conductivity of a two-dimensional graphite system. *Physical Review B*, 65:245420–1–11, 2002.

[63] Y. Zhu, Z. Sun, Z. Yan, Z. Jin, and J. M. Tour. Rational Design of Hybrid Graphene Films for High-Performance Transparent Electrodes. *ACS Nano*, 5:6472–6479, 2011.

[64] P. J. Zomer, S. P. Dash, N. Tombros, and B. J. van Wees. A transfer technique for high mobility graphene devices on commercially available hexagonal boron nitride. *Applied Physics Letters*, 99:232104–1–3, 2011.